



Politecnico di Torino

&

Universidad Politécnica de Madrid

Master's Degree in Mechanical Engineering

A.A. 2025/2026

Master's Thesis

Simulation and experimental characterization of an ion-drag pump geometry optimization

Supervisor:
Prof. Adriano Festa

Candidate:
Michele Blundo

Co-supervisors:
Prof. Mathieu Legrand
Prof. Carmen Martínez Arévalo

June 2026

Abstract

The continuous miniaturization of electronic components and the exponential increase in power density have pushed traditional active cooling solutions to their operational limits. Electrohydrodynamic (EHD) ion-drag pumps have emerged as a promising solid-state alternative, offering silent operation and instantaneous flow control without mechanical moving parts. This thesis presents the comprehensive experimental characterization and analytical modeling of an innovative wire-multiplane ion-drag pump prototype (Notus-3P) intended for hybrid liquid-cooling architectures.

The research is structured around three primary experimental phases. First, an electro-hydraulic characterization evaluates the static pressure generation and current consumption across a 0-20 kV DC voltage sweep, comparing three dielectric fluids: V330, CUTMAX, and OLEON. Second, the practical thermal management capacity of the pump is validated within a hybrid air-liquid loop, utilizing a custom lumped-parameter thermal network model to accurately simulate transient and steady-state temperatures. Finally, a kinematic flow analysis is conducted using non-intrusive Particle Image Velocimetry (PIV) to investigate the internal flow topology.

The results reveal that while pressure and current scale quadratically with voltage in alignment with classic EHD theory, significant kinematic deviations occur in practice. Specifically, PIV analysis of the highly viscous OLEON fluid highlights the formation of three-dimensional secondary structures and pronounced recirculation zones. These phenomena induce severe hydrodynamic energy dissipation, demonstrating that classical one-dimensional theoretical scaling laws consistently overestimate fluid velocity and require explicit empirical calibration factors. Ultimately, this work provides a robust experimental framework validating the multiplane EHD geometry and emphasizing the critical importance of multi-dimensional flow interactions in the design of next-generation solid-state thermal management systems.

Acknowledgments

I would like to express my sincere gratitude to my co-supervisor, Prof. Mathieu Legrand, and to Ph.D. student Alberto Navarro Calvo. Their constant availability, invaluable theoretical insights, and meticulous corrections were fundamental to the development of this thesis. I am especially grateful for their hands-on guidance during the laboratory experiments, their assistance with the measurements and data processing, and their essential support in developing the MATLAB scripts used to generate the graphs and analyze the results.
I would also like to thank my supervisor, Prof. Adriano Festa, and my co-supervisor, Prof. Carmen Martínez Arévalo, for their guidance and support throughout this joint research project between Politecnico di Torino and Universidad Politécnica de Madrid.

Contents

1 Introduction **1**

2 State of the Art **3**
2.1 Fundamentals of Electrohydrodynamics (EHD) 3
2.1.1 Mathematical Antecedents and Analytical Models 4
2.2 Working Fluids in EHD Applications 5
2.3 Thermal Management and Cooling Applications 6
2.4 Experimental Flow Characterization in EHD 7
2.5 Device Under Test: Ion-Drag Pump Prototype 8

3 Pressure and Current Characterization **11**
3.1 Pressure Characterization Setup 11
3.1.1 High Voltage Generation 11
3.1.2 Hydraulic Configuration 11
3.1.3 Experimental Procedure 11
3.1.4 Theoretical Pressure Model 13
3.2 Results and Analysis 15

4 Thermal Characterization **19**
4.1 Thermal Characterization Setup 19
4.1.1 Thermal Test Rig Description 19
4.1.2 Components 20
4.1.3 Instrumentation and Data Acquisition 24
4.1.4 Thermal Model 25
4.2 Results and Analysis 28

5 PIV Flow Characterization **33**
5.1 PIV Characterization Setup 33
5.1.1 Challenges in EHD Applications 33
5.1.2 Tracer Particle Selection 34
5.1.3 FlowMaster Software Calculation Principles 34
5.1.4 Experimental Setup and Processing 36
5.2 Results and Analysis 38
5.2.1 Flow Topology and Secondary Structures 38
5.2.2 Maximum Velocity Characterization 39
5.2.3 Experimental Extraction of the flow-rate 43
5.2.4 Comparison with the Analytical Model 44

5.2.5 Multi-Fluid Kinematic Comparison 47
5.2.6 Volumetric Flow Rate Estimation 47

6 Conclusion **51**

A Matlab Code Snippets **53**

B Experimental Data Tables **62**

List of Figures

2.1 Schematic 3D drawing of the Wire-multiplane geometry (Notus-3P). (a) Side view showing the wire tensioner; (b) Detailed view of the 3-plate collector. Dimensions are in millimeters. 10

3.1 Amprobe 12
3.2 Voltage supply 12
3.3 Experimental setup sketch 12
3.4 Experimental setup in laboratory 12
3.5 Geometric schematic of charge emission from the wire electrode to the collector, highlighting the opening angle β. 16
3.6 Square root of generated static pressure for V330, CUTMAX, and OLEON fluids as a function of applied DC voltage, compared with predicted theoretical trends. 17
3.7 Square root of current intensity for V330, CUTMAX, and OLEON fluids as a function of applied DC voltage, compared with predicted theoretical trends. 17

4.1 Photo of the Corsair Hydro XR5 120 mm radiator used in the prototype. 20
4.2 Description of the loop cooling system combining air and liquid cooling. 21
4.3 Render of the ABS enclosure and the radiator block 22
4.4 Laboratory setup showing the radiator, air outlet, and fluid connections 22
4.5 Render of the CPU heatsink bench with the internal resistor sandwich. There are also cork pannels and cotton to insulate this component 23
4.6 Laboratory setup of the CPU heatsink test bench 23
4.7 Render of the dielectric liquid pump and its internal configuration . . 23
4.8 Laboratory setup showing the steel bench hosting the pump system . 23
4.9 Schematic diagram showing the placement of thermocouples within the cooling loop. 24
4.10 Analytical derivation and mathematical integration of the fluid temperature profile along the heat exchanger length. 26
4.11 Experimental vs. numerical validation of the body and working fluid temperatures at the heat sink over time. 29
4.12 Experimental vs. numerical validation of the dielectric fluid temperature at the radiator inlet and outlet. The dashed lines represent the experimental measurements, while the solid lines depict the theoretical model. 30

4.13 Comparison between experimental data and simulated temperature of the ion-drag pump during the transient heating phase ($M \cdot C_p$ = 1200 J/K, $UA_{loss} = 0.005$ W/K). 32

5.1 Schematic of the PIV image division into interrogation windows . . . 35
5.2 Representation of the cross-correlation peak used to identify the dominant displacement. 35
5.3 Experimental setup sketch 37
5.4 Experimental setup in the laboratory, showing the camera, the laser source, and the EHD prototype 37
5.5 Representative example of the time-averaged two-dimensional velocity field processed via the custom MATLAB script (corresponding to Video 22 at 4000 V, baseline 0° configuration). The vector field and contour levels clearly demonstrate that the fluid flow propagates from right to left, with the superimposed emitter and multiplane collector geometry highlighting the EHD acceleration region and the lateral recirculation zones. 38
5.6 Evolution of the time-averaged axial velocity component (U) at the 0° central plane. The sequence isolates the development of the main EHD jet along the primary pumping direction as the applied voltage increases, providing the quantitative basis for the validation of the 1D analytical model. 40
5.7 Maximum axial velocity (V_{max}) as a function of the applied DC voltage for the OLEON fluid. The experimentally measured PIV data points (markers) for 0° and 30° camera tilts are compared against the adjusted theoretical 1D EHD models ($V_{max,adjusted}$, lines). 41
5.8 Schematic representation of the velocity profile extraction at $x = -8$ mm. The superimposed parabolic curves illustrate the assumed fully developed Poiseuille flow within the upper (v_{up}) and lower (v_{down}) collector channels. 44
5.9 Experimental average axial velocity (V_{media}) for the OLEON fluid at 0° and 30° camera tilts compared against the calibrated theoretical 1D EHD model. 46
5.10 Comparison of the fluid velocity as a function of the applied DC voltage for V330, CUTMAX, and OLEON. The plot highlights the severe discrepancy between the ideal 1D analytical model and the experimental PIV data for the OLEON fluid, indicating the presence of dominant three-dimensional hydrodynamic losses. 48
5.11 Estimated volumetric flow rate (Q) as a function of the applied DC voltage. The experimental data and calibrated 1D EHD theoretical models are compared for the 0° and 30° optical configurations. 49

List of Tables

2.1 Properties of OLEON, CUTMAX and V330 at 25°C 7

4.1 Technical specifications of the proposed liquid cooling radiator. 21
4.2 Variation of the internal thermal conductance UA_{HX} as a function of the mass flow rate for the system components. 27
4.3 Lumped-parameter thermal model baseline properties for the cooling loop components (evaluated at $\dot{m} = 0.0017$ kg/s). 28

5.1 Extracted threshold voltage (V_{SCL}) and charge injection efficiency (η) for the tested dielectric fluids. 45

B.1 Electrical characterization in air 62
B.2 Initial test 63
B.3 Final test 64
B.4 Time evolution test of current and height 65
B.5 PIV experimental data. During the PIV characterization, videos 1 to 12 were recorded with the camera positioned at a 30-degree tilt, whereas for videos 13 to 24, the camera was maintained at 0 degrees. 66

Listings

A.1 Pressure experiment code 53
A.2 PIV experiment code 59

Chapter 1

Introduction

The continuous miniaturization of electronic components and the exponential increase in power density across modern computing architectures have pushed traditional thermal management techniques to their operational limits. Conventional active cooling solutions, relying heavily on mechanical pumps and rotary fans, inherently suffer from mechanical wear, acoustic noise, and vibrations. In this context, Electrohydrodynamic (EHD) ion-drag pumps have emerged as a highly promising solid-state alternative. By leveraging the interaction between intense electric fields and dielectric fluids, EHD devices can generate continuous fluid flow without any moving parts, offering silent operation, instantaneous flow control, and high scalability.

Despite these advantages, the implementation of EHD pumps in commercial cooling loops presents significant engineering challenges. The fluid dynamic performance is highly sensitive to the complex interplay between the electrode geometry and the physicochemical properties of the working fluid. Furthermore, classical one-dimensional theoretical scaling laws often fail to accurately predict the actual kinematic behavior of the fluid, as they neglect severe three-dimensional hydrodynamic losses and secondary flow structures that occur within compact device geometries.

Objective of the Project

The primary objective of this Master's Thesis is the comprehensive experimental characterization and analytical modeling of an innovative wire-multiplane ion-drag pump prototype (the *Notus-3P* model, developed by CEDRION). The study aims to bridge the gap between idealized EHD theoretical scaling laws and the real-world physical behavior of the device when integrated into a liquid-cooling architecture.

To achieve this overarching goal, the research is structured around three specific objectives, which define the core layout of this manuscript:

- **Electro-Hydraulic Characterization (Chapter 3):** To evaluate the static pressure generation and electrical current consumption of the pump across a 0–20 kV DC voltage sweep. This phase involves testing and comparing three different dielectric fluids (V330, CUTMAX, and a newly introduced highly viscous fluid, OLEON) to assess their charge injection efficiency and hydraulic viability.

- **Thermal Management Validation (Chapter 4):** To demonstrate the practical cooling capacity of the EHD pump by integrating it into a hybrid air-liquid thermal loop. A lumped-parameter thermal network model is developed in MATLAB to simulate the transient and steady-state thermal behavior of the system, and subsequently validated against experimental temperature profiles under varying mass flow rates.

- **Kinematic Flow Analysis via PIV (Chapter 5):** To investigate the internal flow topology and quantify the macroscopic fluid velocity using non-intrusive Particle Image Velocimetry (PIV). This advanced optical analysis aims to identify the formation of three-dimensional secondary structures (recirculation zones) and to define the necessary hydrodynamic calibration factors (k_{loss}) required to reconcile the severe kinematic energy dissipation of the OLEON fluid with the idealized 1D theoretical predictions.

Ultimately, this work seeks to provide a robust experimental framework that not only validates the capability of the novel multiplane EHD geometry as an effective fluid driver, but also highlights the critical importance of fluid selection and multi-dimensional flow interactions in the design of next-generation solid-state thermal management systems.

Chapter 2

State of the Art

2.1 Fundamentals of Electrohydrodynamics (EHD)

Electrohydrodynamics (EHD) is the branch of fluid mechanics that studies the interaction between electric fields and dielectric fluids. The fundamental principle underlying this interaction is the generation of a volumetric body force within the fluid, induced by the application of an intense electric field.

The first observations of electrohydrodynamic (EHD) effects date back to 1629, when Cabeo noted that electric fields could attract light particles [6]. In the following centuries, Wilson investigated this phenomenon and coined the term "electric wind" [27]. During the second half of the 19th century, pioneering work by Helmholtz and Smoluchowski described the effect of electric fields on charges within a fluid, establishing the fundamental concepts of electro-osmosis and electrophoresis [25]. A significant theoretical breakthrough occurred in 1961 when Robinson developed a theory on the ion wind and proposed the fabrication of electrostatic blowers, or EHD gas pumps [23]. Although these devices offered advantages such as the absence of mechanical friction and silent operation, their energy conversion efficiency was initially extremely low (less than 1%). During the 1980s and 1990s, the practical interest in EHD pumps transitioned towards the microscale, driven by the advent of MEMS technologies and lab-on-a-chip applications. During the same period, Sharbaugh and Walker were among the first to experiment with EHD pumps using dielectric liquids instead of air, specifically applying them to electric transformers [24].

As classically described by Pickard [19], the electric body force per unit volume $\mathbf{f}_e$ acting on a dielectric fluid can be expressed as the sum of three main components:

$$\mathbf{f}_e = \rho_c \mathbf{E} - \frac{1}{2} E^2 \nabla \epsilon + \frac{1}{2} \nabla \left[\rho \left(\frac{\partial \epsilon}{\partial \rho} \right)_T E^2 \right] \tag{2.1}$$

where ρ_c is the space charge density, $\mathbf{E}$ is the electric field vector, ϵ is the electrical permittivity of the fluid, and ρ is the mass density of the fluid.

The first term of the equation, $\rho_c \mathbf{E}$, represents the *Coulomb force*, which acts on the free charges (ions or electrons) present in the fluid. The second term is the *dielectrophoretic force*, generated by spatial gradients in the fluid's permittivity (a phenomenon typically occurring in the presence of liquid-gas interfaces, bubbles,

or thermal gradients). The third term is the *electrostrictive force*, resulting from variations in permittivity caused by density gradients within the fluid [19].

To generate electric charges within a fluid, three primary methods can be employed: injection (where the electric charge is directly injected into the fluid via electrodes), induction (arising from a conductivity gradient), and conduction (generated by the dissociation of a weak electrolyte in the liquid). The present work focuses on the injection mechanism, which is characteristic of ion-drag pumps.

In EHD ion-drag pumping systems operating with incompressible and isotropic liquids, the predominant mechanism for generating continuous motion is almost exclusively the Coulomb force. As demonstrated in the pioneering studies by Stuetzer [26], when a sufficiently high potential difference is applied between two electrodes (typically asymmetric) immersed in an insulating liquid, a charge injection process is triggered, often through local ionization or the corona effect in the vicinity of the electrode with the highest curvature (the emitter).

The generated ions are accelerated by the electric field toward the ground electrode (the collector). During their transit across the inter-electrode gap, these charges constantly collide with the neutral molecules of the surrounding dielectric fluid. This continuous momentum transfer at the microscopic level translates into a macroscopic pressure generation and a net fluid flow, a phenomenon widely known as ion-drag [26, 20].

In the development of the theoretical framework for ion-drag pumping, Pickard revised and expanded Stuetzer's theories [26], focusing on the "cut-in voltage", which corresponds to the minimum voltage threshold below which the pump does not generate pressure [19, 20]. It is worth noting that the classical dynamic EHD models proposed by Stuetzer and Pickard rely on several simplifying assumptions: the fluid flow is considered laminar, steady, one-dimensional, and incompressible, operating under isothermal conditions.

2.1.1 Mathematical Antecedents and Analytical Models

The fundamental physics of Electrohydrodynamics (EHD) involves a complex coupling between the electrostatic field, charge transport, and fluid motion. The rigorous set of non-linear differential equations governing these phenomena—namely the Navier-Stokes, Gauss law, and charge conservation equations—will be specifically detailed and used to build a semi-empirical simplified model in Section 3.1.4.

Historically, the complete analytical resolution of the EHD coupled problem was difficult to achieve without severe simplifications. The first consolidated theoretical approach for ion-drag pumping was proposed by Stuetzer [26] and later expanded by Pickard [19]. By assuming a one-dimensional, steady-state flow with space-charge-limited emission and neglecting fluid diffusion, Stuetzer demonstrated that the theoretical maximum pressure generation (ΔP_{max}) in an ideal ion-drag pump is proportional to the fluid's permittivity (ϵ) and the square of the applied electric field (E):

$$\Delta P_{max} \approx \frac{1}{2}\epsilon E^2 \tag{2.2}$$

Although this simplified mathematical relation provided the foundation for early

pump designs, it generally overestimated experimental performances since it neglected secondary losses, multi-dimensional fluid flow effects, and the complex nature of the full electrohydrodynamic force [16].

Beyond pressure generation, the transport of charges and the resulting electrical behavior of the fluid were extensively investigated. Atten et al. [2, 3] mathematically categorized the dominance of direct charge injection over pure bulk conduction. Their studies showed how the current density in a dielectric fluid transitions from an Ohmic (linear) regime at low electric fields to a highly non-linear regime at high electric fields, where the injection mechanism actively drives the fluid motion.

To optimize the overall performance and guide the selection of the working fluid, Crowley and Chato [7] developed an analytical model evaluating the thermodynamic efficiency of EHD pumps. They defined the theoretical maximum efficiency (η_{max}) in relation to the fluid's macroscopic velocity (u) and the ionic drift velocity ($\mu_{ion}E$, where μ_{ion} is the ionic mobility):

$$\eta_{max} \approx \frac{u}{u + \mu_{ion}E} \tag{2.3}$$

This critical mathematical condition highlights that high efficiency is achieved only when the fluid velocity is comparable to or exceeds the ionic drift. Consequently, modern EHD pump designs and experimental characterizations [5] prioritize working fluids with low electrical conductivity and low ionic mobility to minimize Ohmic losses and maximize the electrokinetic energy conversion.

2.2 Working Fluids in EHD Applications

The performance of an electrohydrodynamic ion-drag pump is fundamentally dictated not only by the electrode geometry but also by the physicochemical properties of the dielectric working fluid. The complex interplay between fluid dynamics and electrostatics requires a careful evaluation of the fluid's intrinsic characteristics.

In a seminal theoretical study, Crowley et al. [7] established the criteria for selecting an optimal working fluid to maximize both the flow rate and the overall pumping efficiency. According to their analysis, the pumping efficiency is heavily dependent on the ionic mobility (K) of the charge carriers within the fluid, a parameter that is typically estimated analytically via the Walden rule due to the complexity of direct experimental measurements. To achieve high efficiency, a fluid should ideally possess a low ionic mobility coupled with a high electrical permittivity (ϵ). To quantify this, Crowley introduced the concept of hydrodynamic mobility, defined as $K_H = \sqrt{\epsilon/\rho}$ (where ρ is the fluid density), demonstrating that the pump's performance scales favorably with the mobility ratio $M = K_H/K$ [7].

However, theoretical models must be carefully reconciled with experimental realities, as dielectric fluids are subjected to extreme electrical and thermal stresses during operation. Bryan and Seyed-Yagoobi [5] conducted extensive experimental investigations using various working fluids, including dodecylbenzene and several silicone oils, to evaluate their practical viability for ion-drag pumping.

Their findings highlighted that kinematic viscosity and electrical conductivity significantly influence the maximum static pressure generation and the drawn elec-

trical current. Fluids with higher viscosity naturally present greater hydrodynamic resistance to flow, whereas excessive intrinsic electrical conductivity (σ) can lead to severe Ohmic losses, bypassing the ion-drag mechanism and drastically reducing the overall efficiency [5].

Furthermore, Bryan's experimental work emphasized the critical issue of fluid stability over time. Under prolonged exposure to high-voltage corona discharges, dielectric fluids can undergo chemical and thermal degradation. The introduction of impurities, such as absorbed moisture or molecular breakdown byproducts, can drastically alter the fluid's conductivity and lower its dielectric strength. This degradation ultimately limits the maximum applicable voltage and can lead to premature electrical arcing, which may physically damage the pump electrodes [5].

Beyond electrical and hydrodynamic considerations, the selection of an appropriate working fluid must also satisfy several practical constraints. Particularly, the selected medium must exhibit high *chemical compatibility* with the materials constituting the pump, as certain fluids can induce corrosion or damage internal components over time [4]. Furthermore, *thermal stability* is crucial; the fluid must be able to withstand the temperature ranges specific to the application without undergoing thermal decomposition or significant alterations in its physicochemical properties [13]. Finally, for safety and operability reasons, ideal working fluids should possess low flammability, low vapor pressure (to prevent evaporation), and pose no toxicity hazards to human health or the environment.

These rigorous physical, electrical, and practical constraints justify the careful selection of specialized commercial dielectric oils and synthetic heat transfer fluids. In this study, fluids engineered with high dielectric strength and specific viscosity profiles—namely the OLEON, CUTMAX, and V330 variants—are investigated to ensure reliable, stable, and efficient EHD operation.

To properly evaluate these fluids against Crowley's criteria, it is necessary to define their specific parameters. A critical physical parameter for this analysis is the ionic mobility, K, which defines the maximum relative velocity of charge carriers with respect to the fluid, constrained by molecular viscous drag. Given the difficulties in experimentally measuring ionic mobility, it has been estimated using the Walden rule [8], assuming Stokes drag: $K = 2 \cdot 10^{-11}/\mu$.

Similarly, the DC electric conductivity, σ, is rarely specified due to its extremely low magnitude and high sensitivity to fluid purity and moisture. Consequently, σ is calculated using the estimation method proposed in [15]:

$$\sigma = \sqrt{c_w} \cdot 10^{-2.34}\, 10^{-\frac{20.8}{\epsilon_r}} \tag{2.4}$$

where $c_w = 10^{-4}$ mol/L represents the assumed water concentration when exact data is unavailable. Fluid density and dynamic viscosity values correspond to manufacturer data at 25°C.

2.3 Thermal Management and Cooling Applications

The continuous miniaturization of electronic components and the exponential increase in the power density of modern processors (CPUs and GPUs) have pushed

Table 2.1: Properties of OLEON, CUTMAX and V330 at 25°C

Liquid	**Density** ρ_f [kg/m^3]	**Visc.** μ [mPa·s]	**Diel. cte.** $\epsilon_r = \epsilon/\epsilon_0$ [-]	**Cond.** σ [S/m]	**Ionic mob.** K [m^2/Vs]	**Hydr. mob.** $K_H = \sqrt{\frac{\epsilon}{\rho}}$ [m^2/Vs]	**Vel. ratio** $M = K_H/K$ [-]
OLEON	856	7.5	3.2	$1.44 \cdot 10^{-11}$	$2.95 \cdot 10^{-9}$	$1.82 \cdot 10^{-7}$	61.69
CUTMAX	780	2	2	$1.82 \cdot 10^{-15}$	$7.94 \cdot 10^{-9}$	$1.51 \cdot 10^{-7}$	18.98
V330	860	3.2	3.2	$1.45 \cdot 10^{-11}$	$6.54 \cdot 10^{-9}$	$1.80 \cdot 10^{-7}$	27.77

traditional thermal management techniques to their operational limits. In this context, electrohydrodynamic (EHD) pumps have emerged as a highly promising alternative to conventional mechanical cooling systems [11].

Compared to traditional mechanical pumps and fans, EHD ion-drag pumps offer several distinct advantages. Primarily, they operate entirely without moving parts, which inherently eliminates mechanical wear, reduces maintenance requirements, and ensures completely silent operation [11]. Furthermore, the fluid flow can be directly and instantaneously controlled by simply modulating the applied electric voltage, allowing for smart, adaptive cooling systems that respond in real-time to the thermal load of the processor. This absence of mechanical vibrations also makes EHD systems highly attractive for aerospace and microgravity applications, where mechanical disturbances must be strictly minimized.

Beyond merely circulating the coolant, the application of high-intensity electric fields actively enhances the convective heat transfer process. The injection of charges and the resulting ion-drag phenomenon induce secondary flows and electroconvective vortices within the dielectric fluid. These secondary motions effectively destabilize and thin the thermal boundary layers adjacent to the heat transfer surfaces, leading to a significant increase in the local heat transfer coefficient compared to standard forced convection [13].

Additionally, EHD technology is highly scalable. While historically explored for cooling macroscopic high-voltage equipment such as oil-filled power transformers [24], modern focus encompasses an extremely wide range of scales. As demonstrated by the computational and experimental work of Darabi and Rhodes [11], ion-drag micropumps can be directly integrated into micro-channels or chip-cooling systems to handle high heat fluxes. At the other end of the spectrum, the same EHD principles can be scaled up to macroscopic liquid-air heat exchangers (such as the bespoke radiator setup used in this thesis), providing a versatile and robust solution for advanced hybrid thermal management.

2.4 Experimental Flow Characterization in EHD

Accurately measuring the velocity field of a fluid driven by electrohydrodynamic forces presents a unique set of experimental challenges. Traditional invasive measurement devices, such as Pitot tubes or hot-wire anemometers, are fundamentally unsuitable because their metallic or physical presence heavily distorts the high-intensity electric field and disrupts the delicate charge injection mechanisms.

To overcome this, non-intrusive optical measurement techniques, particularly Particle Image Velocimetry (PIV), have become the standard in EHD research. PIV allows for the extraction of instantaneous, two-dimensional velocity fields without physically interfering with the fluid flow or the electric field lines.

However, applying PIV to EHD flows introduces a critical source of potential error. The technique relies on dispersing micro-particles (tracers) into the fluid and tracking their motion using laser sheets and high-speed cameras. In the presence of strong electric fields and corona discharges, these tracer particles can inadvertently acquire a net electric charge. Once charged, the particles are subjected to a direct Coulomb force (and potentially dielectrophoretic forces) that causes them to migrate relative to the surrounding fluid. This phenomenon, known as electrophoretic migration, means that the particles no longer faithfully follow the fluid streamlines, leading to an overestimation or misrepresentation of the actual fluid velocity.

As recently highlighted in the state-of-the-art analysis by Daaboul and Louste [10], validating PIV measurements in EHD flows requires an extremely careful selection of seeding particles and their optimal seeding density. Researchers must evaluate the material's dielectric properties, electrical conductivity, and particle diameter. To mitigate parasitic electrical forces, the ideal tracer particles should possess very low electrical conductivity and a dielectric permittivity closely matching that of the working fluid, thereby minimizing dielectrophoretic effects. Common choices include polyamide particles or hollow glass spheres. The ultimate goal is to optimize the Stokes number while ensuring that the aerodynamic drag force exerted by the fluid remains orders of magnitude larger than the parasitic Coulomb force, thereby minimizing the velocity slip between the tracer and the dielectric liquid.

Furthermore, acquiring high-fidelity experimental data through an optimized PIV setup is indispensable for the validation of computational models. Given the highly non-linear coupling between the fluidic Navier-Stokes equations and the electrostatic charge conservation equations, numerical simulations of EHD pumps often rely on necessary simplifying assumptions. By rigorously comparing computationally derived velocity profiles with experimental PIV vector fields, researchers can iteratively tune their CFD models, quantify vectorial error margins, and ensure an accurate representation of the complex multi-physics phenomena driving the ion-drag pump.

2.5 Device Under Test: Ion-Drag Pump Prototype

The electrohydrodynamic (EHD) device employed in this study, designated as the "Notus-3P" model, was developed and supplied by CEDRION [21]. It features a wire-multiplane geometry designed to balance charge injection efficiency with hydraulic performance. The schematic representation of the device is shown in Figure 2.1.

The pump assembly comprises three main subsystems:

1. **Emitter Electrode:** The corona discharge is initiated by a high-purity (99.95%) tungsten wire with a diameter of 50 µm. During operation, this electrode functions as the positive electrode, maintained at a high positive DC voltage

ranging from 1 kV to 20 kV. To ensure a uniform electric field distribution, the wire is mechanically tensioned at one end (see Fig. 2.1a). This tensioning mechanism maintains a constant inter-electrode gap of 3.5 mm between the wire and the tip of the grounded collector throughout the entire active length.

2. **Collector (Ground) Electrode:** The counter-electrode is a lightweight aluminum structure with a total mass of 1.7 g. Its overall dimensions are 35 mm in width, 7 mm in height, and 8 mm in length. The geometry consists of three parallel metallic planes, each 1 mm thick, spaced 2 mm apart. These gaps allow the dielectric fluid to flow through the electrode with minimal hydraulic resistance.

   A critical design feature is the rounding of the plate edges facing the emitter. This surface smoothing is essential to prevent local electric field amplification, which would otherwise lead to premature electrical breakdown in the fluid, thereby limiting the maximum operational voltage. The plates are structurally supported by two lateral frames (cross-section 2×2 mm) at the ends,opposite to the emitter wire, resulting in a net flow width of 31 mm at the outlet. This component acts simultaneously as the electrical ground and as the sink for the charge carriers, driving the EHD acceleration within the inter-electrode region.

3. **Support Frame and Casing:** The electrode assembly is encapsulated within a bracket structure manufactured from Acrylonitrile Butadiene Styrene (ABS) via Fused Deposition Modeling (FDM) 3D printing. ABS was selected for its electrical insulation properties ($\sigma_{ABS} \approx 10^{-13}$ S/m and $\epsilon_{r,ABS} \approx 4.0$ at 0.01 Hz and 30 °C [17]). This casing serves multiple functions: it secures the components, isolates the high voltage, and confines the electric field lines within the ion-drag region.

   The flow channel geometry expands along the flow direction. The rectangular inlet section, adjacent to the tungsten wire, has a cross-section of $H \times W = 6.5 \times 25\,\text{mm}^2$, while the outlet section expands to $7 \times 35\,\text{mm}^2$ to accommodate the collector geometry.

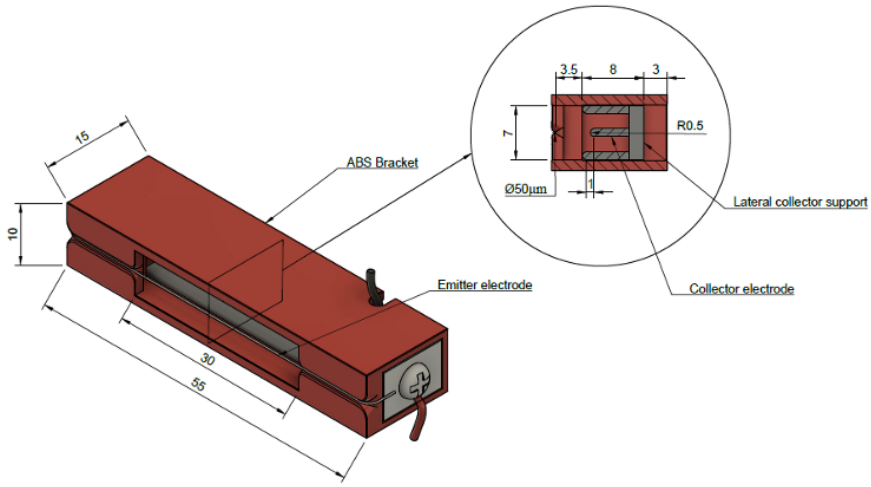


Figure 2.1: Schematic 3D drawing of the Wire-multiplane geometry (Notus-3P). (a) Side view showing the wire tensioner; (b) Detailed view of the 3-plate collector. Dimensions are in millimeters.

Chapter 3

Pressure and Current Characterization

3.1 Pressure Characterization Setup

A dedicated setup was built to evaluate the hydraulic performance of the pump, with the specific objective of measuring both the generated maximum static pressure head and the consumed current.

3.1.1 High Voltage Generation

The device was powered by a Heizinger PCN-20000-10pos high-voltage source (Fig. 3.2), which allows for a DC voltage sweep ranging from 0 to 20 kV. To measure the current intensity (I), an Amprobe 37XR-A multimeter (Fig. 3.1) with a resolution of 0.01 μA was connected in series with the circuit, as shown in Fig. 3.3.

3.1.2 Hydraulic Configuration

The pump, described in 2.5, is submerged in a reservoir containing the dielectric fluid. To measure the static pressure generation, the pump outlet is connected via an adapter to a vertical piezometric tube composed of borosilicate glass. The static pressure (ΔP) is determined by measuring the hydrostatic column height (ΔH) achieved by the fluid, according to the equation:

$$\Delta P = \rho \cdot g \cdot \Delta H \tag{3.1}$$

3.1.3 Experimental Procedure

The experimental procedure consists of increasing the applied voltage in discrete steps. For each voltage level, the liquid column is allowed to stabilize before recording the height.

First, we perform an electrical characterization in air (the complete dataset is reported in Appendix B, Table B.1). This preliminary step is crucial to establish a baseline for the electrode configuration, verify the circuit's integrity, and measure



Figure 3.1: Amprobe



Figure 3.2: Voltage supply

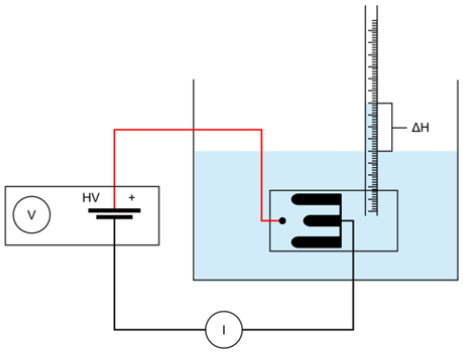


Figure 3.3: Experimental setup sketch

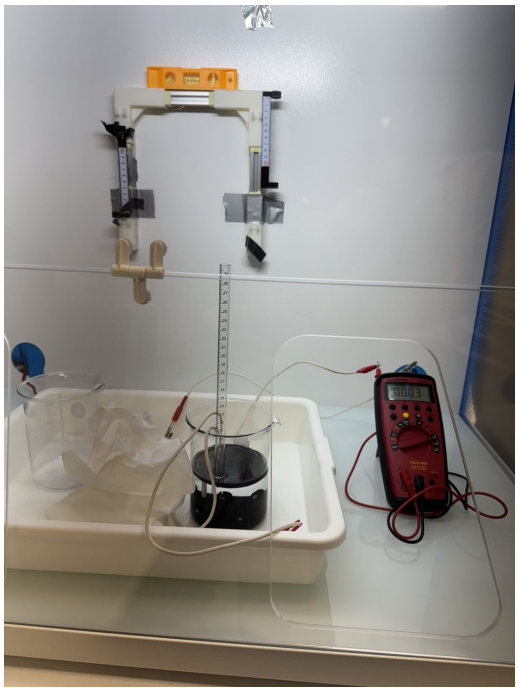


Figure 3.4: Experimental setup in laboratory

any baseline leakage currents before the working fluid is introduced. During this phase, the applied voltage strictly never exceeds 8 kV to prevent electrical breakdown. Breakdown occurs when the electric field becomes strong enough to ionize the air, creating a sudden conductive path (an electrical arc). The intense localized heat generated by this arcing can physically damage or snap the thin wire electrode of the EHD pump.

After this baseline characterization, we add the dielectric fluid (approximately 310 mL) and seal the container with a black cap to prevent the fluid from oxidizing and to avoid the formation of air bubbles. Then, we begin measuring the current and ΔH, as shown in Table B.2.

Following this, a time-dependent evolution test is conducted (Table B.4). This involves measuring the current and ΔH at specific intervals: every 0.5 min up to 5 min, then every 1 min up to 10 min, and finally every 5 min up to 60 min. This test is performed at a constant voltage of 15 kV to observe how the progressive degradation of both the dielectric fluid and the pump electrodes over time affects the measurement of these two variables. Finally, the initial step-voltage test is repeated to evaluate the system's performance after prolonged use (Table B.3).

It should be noted that in calculating the pressure using Equation 3.1, a density (ρ_f) value of 808 kg/m^3 was used. This value was obtained by calculating it with a mass of 250.6 g and a volume of 310 mL.

3.1.4 Theoretical Pressure Model

The operation of an electrohydrodynamic (EHD) pump is based on the interaction between an electric field and a dielectric fluid. The governing physics are described by a coupled system of fluid dynamics and electrostatic equations. Assuming steady-state operation, the quasi-electrostatic equations lead to Gauss's law and Poisson's equation:

$$\begin{cases} \nabla \cdot (\epsilon \mathbf{E}) = \rho \\ \mathbf{E} = -\nabla V \end{cases} \implies \nabla^2 V = -\frac{\rho}{\epsilon} \tag{3.2}$$

where ρ is the free space charge density (C/m^3), and $\mathbf{E}$ and V are the electric field and electric potential, respectively. Simultaneously, under the assumed steady-state conditions, the fluid motion is governed by the Navier-Stokes equations for an incompressible, steady Newtonian fluid with density ρ_f and dynamic viscosity μ:

$$\rho_f(\mathbf{u} \cdot \nabla)\mathbf{u} = -\nabla p + \mu \nabla^2 \mathbf{u} + \mathbf{f}_e + \rho_f \mathbf{g} \tag{3.3}$$

The key coupling between the electric and velocity fields is the electrical body force density $\mathbf{f}_e$, which acts upon the fluid:

$$\mathbf{f}_e = \rho \mathbf{E} - \frac{1}{2} E^2 \nabla \epsilon + \frac{1}{2} \nabla \left[E^2 \rho_f \left(\frac{\partial \epsilon}{\partial \rho_f} \right) \right] \tag{3.4}$$

The first term, $\rho \mathbf{E}$, is the Coulomb force, acting on the free electric charges present in the fluid. The second term is the dielectrophoretic force, arising from gradients in the electrical permittivity of the medium ($\nabla \epsilon$). The third term is the

electrostriction force, related to the variation of permittivity due to changes in fluid density. For ion-drag pumping in an incompressible liquid, the Coulomb force is the dominant mechanism driving permanent motion; thus, it is generally assumed that $\mathbf{f}_e \approx \rho\mathbf{E}$.

Furthermore, in a steady-state regime, charge conservation requires $\nabla \cdot \mathbf{j} = 0$, where $\mathbf{j}$ is the current density ($\mathrm{A/m^2}$). The current intensity circulating within the fluid is driven by four main mechanisms: diffusion of charged species (which is negligible), ion migration due to the electric field, charge transport swept by the fluid flow, and intrinsic conduction. In dielectric liquids, the intrinsic conductivity (σ) is very low and often neglected. Therefore, the current density can be approximated as:

$$\mathbf{j} = \rho(K\mathbf{E} + \mathbf{u}) + \sigma\mathbf{E} \tag{3.5}$$

where K is the ionic mobility of the charge carriers in the fluid. Applying these simplifications allows for the derivation of scaling laws to a priori estimate the pump's performance trends:

- **For maximum pressure head:** Assuming a large electric potential V and minimal velocities ($\mathbf{u} \approx 0$ at the pump inlet/outlet), Equation 3.3 simplifies to $\nabla p \approx \rho\mathbf{E}$. In an ion-drag pump, the Space Charge Limited (SCL) approximation is often employed: $\rho_{SCL} \approx \epsilon E_0/L$ [7], where E_0 is the homogeneous electric field V_0/L. However, classical SCL theory assumes perfect injection starting from zero voltage. Experimental evidence indicates that for certain dielectric liquids, a threshold voltage (V_{SCL}) is required to initiate the ion-drag mechanism. Incorporating an efficiency factor (η) to model the fluid's ability to generate free charges, the space charge density scales as:

  $$\rho^* \sim \eta\epsilon\frac{V_0 - V_{SCL}}{L^2} \tag{3.6}$$

  Between the electrodes, the fluid might not be entirely at rest; thus, the following equation provides a higher estimate of the maximum pressure head generated by the pump:

  $$\Delta p^* = \eta\epsilon V_0\frac{V_0 - V_{SCL}}{L^2} \tag{3.7}$$

- **For maximum flow rate:** During maximum flow operation, the pressure head provided by the pump compensates for internal losses ($\Delta p/L \approx 0$), leading to the velocity scaling law:

  $$u^* = \sqrt{\frac{\eta\epsilon}{\rho_f}}\frac{\sqrt{V_0(V_0 - V_{SCL})}}{L} = K_H\sqrt{\eta\frac{V_0 - V_{SCL}}{V_0}}\left(\frac{V_0}{L}\right) \tag{3.8}$$

  where $K_H = \sqrt{\epsilon/\rho_f}$ is the hydrodynamic mobility. In the ion-drag regime for liquids, the mobility ratio is typically $M = K_H/K \gg 1$.

- **For total current:** Similarly, neglecting intrinsic conductivity in Equation 3.5 yields the scaling law for current density:

$$j^* = \frac{\eta\epsilon(V_0 - V_{SCL})}{L^2}\left[K + K_H\sqrt{\eta\frac{V_0 - V_{SCL}}{V_0}}\right]\frac{V_0}{L} + \sigma\frac{V_0}{L} \tag{3.9}$$

The total current intensity I can be derived from the current density vector $\mathbf{j}$ by considering the geometry of the emission system (see the sketch in Figure 3.5). Formally, evaluating the arrival of charges at the collector, the total current is defined as the surface integral of the current density over the effective cross-sectional area A:

$$I = \int_A \mathbf{j} \cdot d\mathbf{A} \tag{3.10}$$

Considering the macroscopic footprint of the flow directly on the collector, the effective area can be simply estimated as a rectangle of width w (depth or effective length of the electrode) and height h:

$$A \approx w \cdot h \implies j^* \approx \frac{I}{w \cdot h} \tag{3.11}$$

However, a more physically rigorous analysis requires modeling the emission from the wire to the collector. The charges do not travel in perfectly parallel lines but undergo a fan-like expansion subtending a certain opening angle β.

At a generic radial distance r from the emitting wire, the area crossed by the charge corresponds to a cylindrical surface sector. Knowing that the total lateral area of a cylinder is $2\pi rw$, the fraction of the surface actually affected by the emission is determined by the ratio between the opening angle and the full angle ($\frac{\beta}{2\pi}$). Therefore, the area for the current passage is:

$$A = \frac{\beta}{2\pi}(2\pi rw) = \beta rw \tag{3.12}$$

Substituting this expression into Equation 3.10 yields the relationship for the current intensity as a function of the emission angle and the radial distance:

$$I = j^* \cdot \beta rw \approx j^* \cdot hw \tag{3.13}$$

Evaluating this equation near the collector, i.e., setting $r = L$ (where L is the distance between the emitting electrode and the collector), the length of the circular arc affected by the flow is equal to βL. If the charge flow exactly covers the receiving area, the geometric approximation $h \approx \beta L$ holds, demonstrating the consistency between the rigorous cylindrical sector model and the simpler macroscopic rectangular approximation illustrated previously.

3.2 Results and Analysis

The following section presents the experimental results regarding the pressure generation and current consumption of the pump. The graphs illustrate the trends

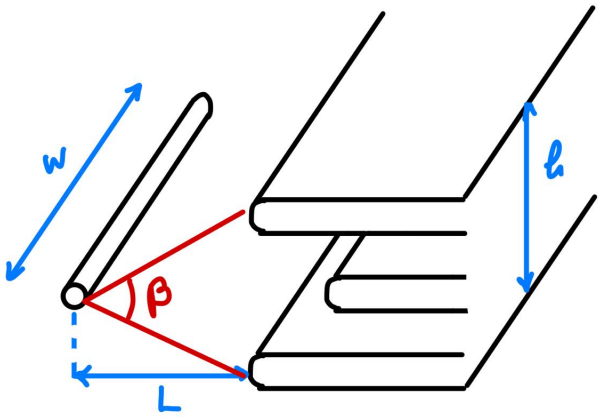


Figure 3.5: Geometric schematic of charge emission from the wire electrode to the collector, highlighting the opening angle β.

of these variables as a function of the applied DC voltage, comparing the newly tested dielectric fluid, OLEON, with two other established dielectrics: V330 and CUTMAX. For each type of dielectric fluid, the experimental values are plotted alongside their corresponding theoretical models.

For the theoretical pressure model, Eq. 3.7 was utilized, while the current model was evaluated using Eq. 3.13.

To ensure that the model accurately matches the experimental data, the charge injection efficiency (η) and the threshold voltage for space charge limit (V_{SCL}) were iteratively tuned. The specific parameters utilized for V330, CUTMAX, and OLEON were derived from the simultaneous multi-variable regression detailed later in Section 5.2.4. A comprehensive summary of these extracted values is provided in Table 5.1.

As can be observed in Figure 3.6 and Figure 3.7, both the square root of the pressure and the square root of the current exhibit a nearly linear relationship with the applied voltage. This confirms that both macroscopic quantities scale with the square of the voltage (V_0^2), aligning seamlessly with the theoretical scaling laws for EHD flows operating in the ion-drag regime.

Although all three fluids follow the characteristic quadratic trend, their overall performances vary significantly due to their intrinsic physicochemical properties. The V330 fluid demonstrates vastly superior performance, which is physically justified by its high relative permittivity ($\epsilon_r = 3.2$) and a remarkably high charge injection efficiency ($\eta = 0.9$), coupled with a low injection threshold ($V_{SCL} = 1.0$ kV). This combination allows for immediate and robust momentum transfer from the very onset of voltage application.

Conversely, the OLEON fluid exhibits a much lower charge injection efficiency ($\eta = 0.3$) despite sharing the same relative permittivity as V330 ($\epsilon_r = 3.2$). Its threshold voltage ($V_{SCL} = 1.5$ kV) is lower than that of CUTMAX ($V_{SCL} = 2.5$ kV), which explains why OLEON begins to generate measurable pressure at lower voltages. However, because CUTMAX possesses a higher injection efficiency ($\eta = 0.6$), its theoretical and experimental performance curves present a steeper slope,

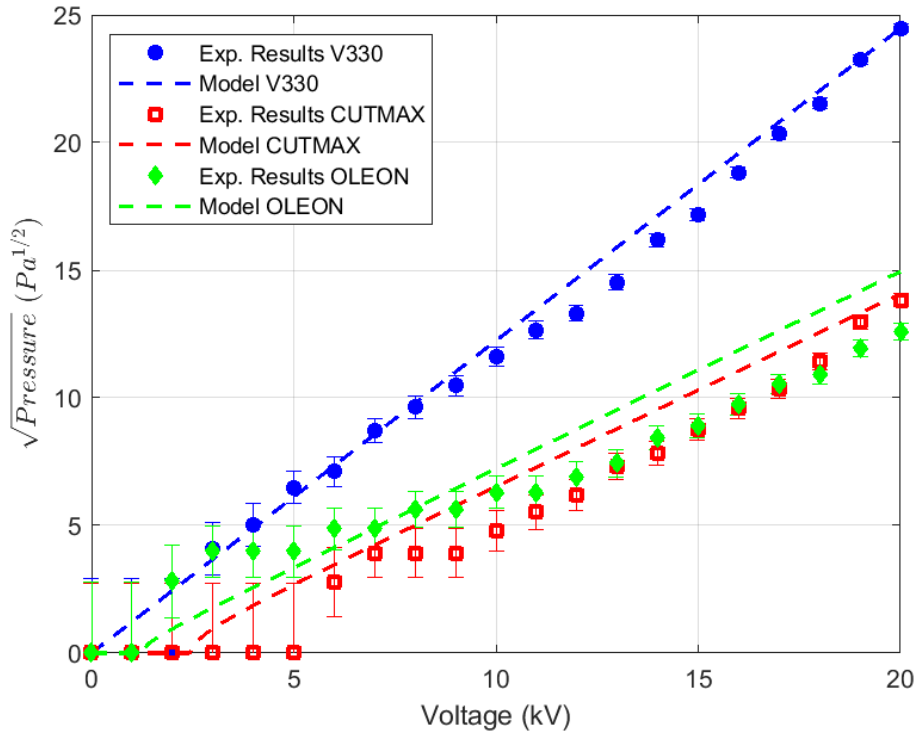


Figure 3.6: Square root of generated static pressure for V330, CUTMAX, and OLEON fluids as a function of applied DC voltage, compared with predicted theoretical trends.

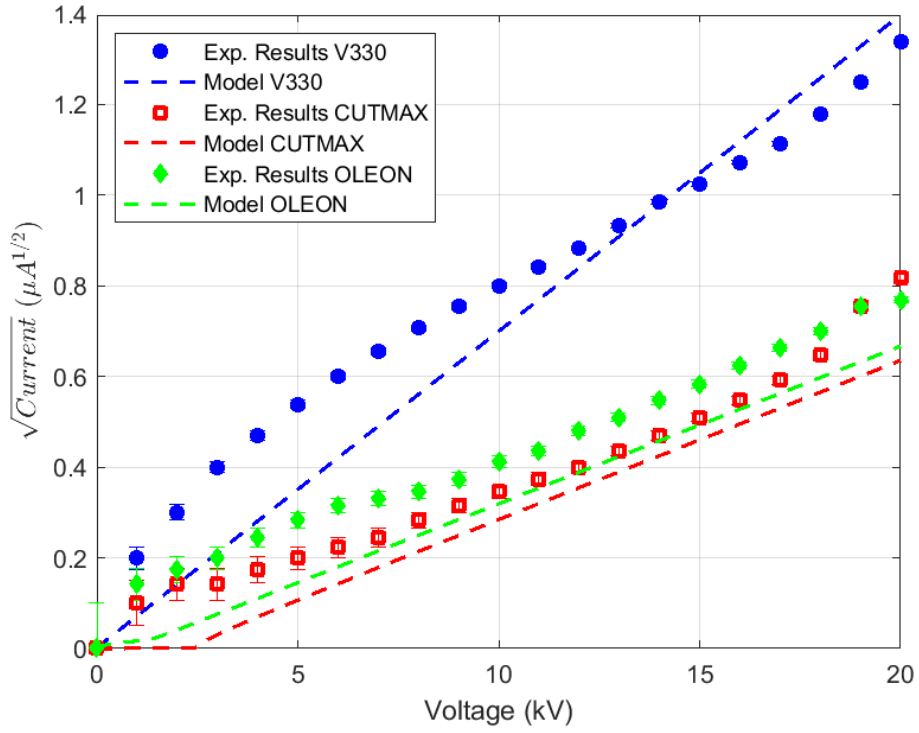


Figure 3.7: Square root of current intensity for V330, CUTMAX, and OLEON fluids as a function of applied DC voltage, compared with predicted theoretical trends.

eventually catching up to OLEON at higher voltages.

Finally, it is essential to note that while the general trend aligns well with the theoretical models (represented by the dashed lines), the experimental values slightly deviate from and fall below the dimensional estimates at higher voltages for all fluids. This discrepancy can be attributed to secondary factors not accounted for in the simplified 1D analytical model, such as internal hydrodynamic viscous losses across the multiplane collector and potential early-stage degradation of the fluid under prolonged high-voltage exposure.

Chapter 4

Thermal Characterization

4.1 Thermal Characterization Setup

This section describes the experimental facility used to evaluate the cooling capacity of the pump.

4.1.1 Thermal Test Rig Description

The primary objective is the development of a laboratory-scale air-liquid cooling prototype capable of dissipating a thermal load of 30 W with a target temperature difference (ΔT) of 30°C, leveraging the EHD technology developed by CEDRION.

The preliminary analysis of the essential components required for the experimental setup yielded the following hardware selection:

- A standard liquid/air radiator designed for CPU or GPU heat dissipation.
- A CPU heatsink block coupled with resistive heating elements to simulate the thermal load (test bench).
- Tubing for fluid distribution throughout the hydraulic circuit.
- Valves and necessary fittings to establish secure connections within the loop.
- Temperature sensors (thermocouples/probes) for data acquisition.
- The conventional rotary fan is replaced by an ionic wind pumping system designed by CEDRION, based on their proprietary Notus technology.
- A custom EHD pump, also based on Notus technology, specifically engineered for this project previously described in section 2.5.

It is crucial to distinguish the specific roles of the two distinct media employed in this hybrid cooling architecture. The liquid coolant acts as the primary heat transport medium, circulating within the hermetically sealed hydraulic circuit to transfer thermal energy from the heat source to the radiator. Conversely, the term plasma in this context refers to the Electrohydrodynamic (EHD) phenomenon known as ionic wind. Generated by high-voltage electrodes external to the hydraulic loop, this

plasma-driven airflow replaces the conventional mechanical fan. It induces forced convection over the corrugated air channels of the radiator, thereby dissipating heat from the internal liquid to the ambient environment without direct physical contact between the plasma and the liquid coolant.

The following section details the sizing procedure for the closed-loop cooling circuit, based on the hybrid air-liquid plasma cooling technology. To facilitate the experimental implementation, the setup was designed to emulate a commercial desktop liquid cooling architecture. The system comprises a custom injection pump operating with V330 dielectric fluid, a radiator equipped with a cooling fan, and a thermal block coupled to the CPU, through which the heat transfer fluid circulates. This configuration was essential for validating the thermal performance of the system.

Figure 4.2 illustrates the schematic of the cooling loop intended for dimensioning. To optimize the preliminary calculation process, geometric parameters were derived from the Corsair Hydro X Series XR5 (120 mm) radiator model. Furthermore, the hydraulic circuit constraints were defined to include 3 meters of flexible PVC tubing with an inner diameter of 11 mm, along with a heatsink characterized by 10 mm internal channels and three 180° return bends.

The technical specifications of the selected commercial liquid-air radiator are summarized in Table 4.1. A visual representation of the component is provided in Figure 4.1.



Figure 4.1: Photo of the Corsair Hydro XR5 120 mm radiator used in the prototype.

Specifically, the internal core of the radiator features a structure of parallel flat brass channels for the liquid flow, interconnected by a dense network of folded copper corrugated air channels with a density of 16 FPI (Fins Per Inch), maximizing the surface area available for air-side heat transfer.

4.1.2 Components

Concurrent with the design phase, manufacturing trials were conducted to verify geometric tolerances, assess component fits, and evaluate the assembly feasibility regarding cabling, sensors, and external peripherals.

Table 4.1: Technical specifications of the proposed liquid cooling radiator.

Model	**Material**	**Type**	**Dimensions** [mm]	**Fittings**
Corsair Hydro X Series, XR5 (120 mm)	Copper	Corrugated panel channels	$160 \times 120 \times 30$	Ø 12.7 mm

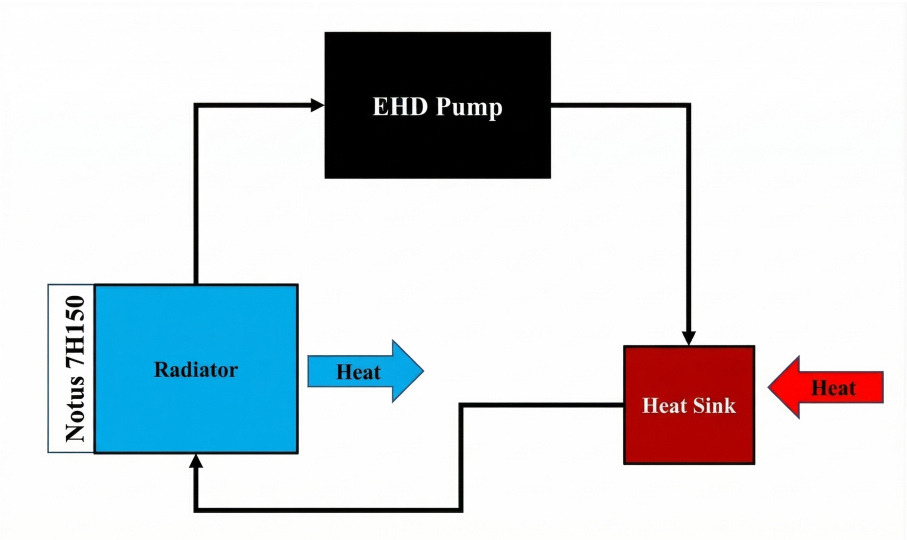


Figure 4.2: Description of the loop cooling system combining air and liquid cooling.

The following sections present a comprehensive evaluation of the prototype's construction elements, detailing the evolution of the design and the fine-tuning of individual subsystems. Furthermore, the results of material compatibility and leak integrity tests, crucial for establishing a functional prototype ready for validation benchmarks, are discussed below.

Radiator

The radiator chosen for the system is a commercial model (Corsair Hydro X Series, 120 mm XR5). A ventilation system consisting of two Notus 7H150 devices was mounted on it. The coupling between the radiator and the Notus devices was achieved using a custom-designed enclosure, 3D printed using ABS filament. The component was also instrumented with thermocouples to measure the temperature of the outlet air and the liquid entering and exiting the radiator.

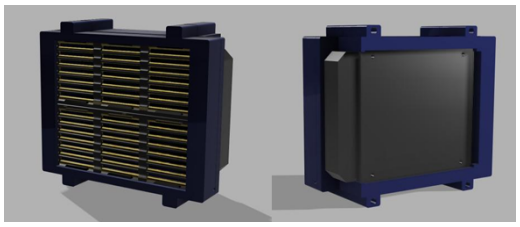


Figure 4.3: Render of the ABS enclosure and the radiator block

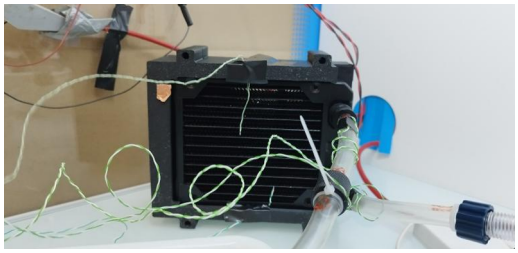


Figure 4.4: Laboratory setup showing the radiator, air outlet, and fluid connections

CPU Heatsink and Resistance

To simulate the thermal load, a specific test bench for the heater was designed and 3D printed. This bench houses the heatsink itself, two 50W resistors, and ceramic fiber thermal insulation to reduce heat loss to the outside. The flat plane resistance was clamped to the heatsink using screws and MX-2 thermal paste to ensure optimal thermal contact, with a thermocouple placed in between for continuous temperature monitoring. The hydraulic connections were made with flexible PVC piping, carefully sealed with Teflon tape and plastic zip ties.

Dielectric Liquid Pump

The dielectric liquid pump represents the most complex component of the system, having required multiple design iterations to overcome construction challenges. A detailed description of the type of pump used in this setup can be found in Section 2.5. Due to difficulties in ensuring a watertight seal using exclusively 3D printed materials (ABS), the final version employs a steel and methacrylate test bench. This metal structure was externally covered with cork and thermal insulation tape to prevent heat loss. In this configuration, two pumps were placed in parallel to manage the fluid flow. Furthermore, the pumping system consisted of three stages in series, although one of them was kept deactivated during the experiments.

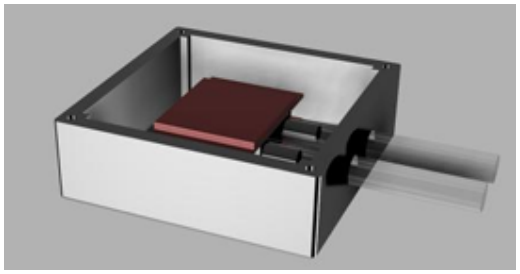


Figure 4.5: Render of the CPU heatsink bench with the internal resistor sandwich. There are also cork pannels and cotton to insulate this component



Figure 4.6: Laboratory setup of the CPU heatsink test bench

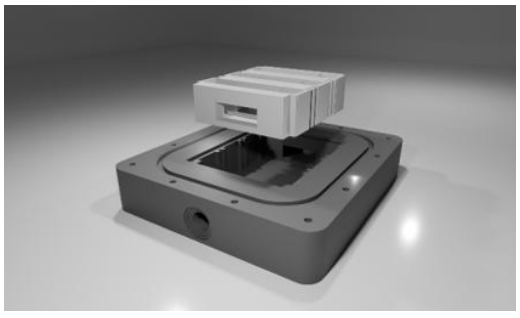


Figure 4.7: Render of the dielectric liquid pump and its internal configuration

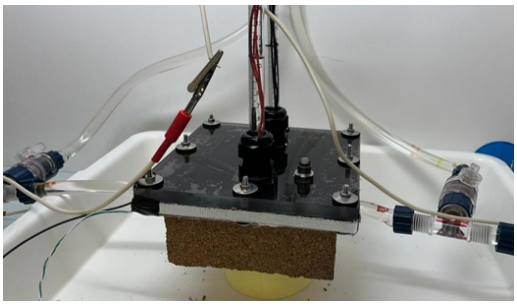


Figure 4.8: Laboratory setup showing the steel bench hosting the pump system

4.1.3 Instrumentation and Data Acquisition

To effectively monitor the experimental parameters, the circuit has been instrumented with a comprehensive array of thermal sensors and auxiliary pressure measurement devices.

Thermocouples have been strategically positioned at key locations within the system to characterize the thermal performance:

- **CPU Heatsink:** Inlet and outlet ports.
- **Oil Loop Radiator:** Inlet and outlet ports.
- **Ambient:** One thermocouple positioned to record the reference ambient temperature.
- **Radiator Air Exhaust:** Two thermocouples placed at the air outlet of the radiator.
- **External Pump:** One thermocouple located on the pump housing/bench.
- **Heat Source:** One thermocouple positioned at the interface between the heating resistors and the heatsink (representing the hot spot).

Figure 4.9 illustrates the schematic arrangement of these thermocouples within the cooling loop.

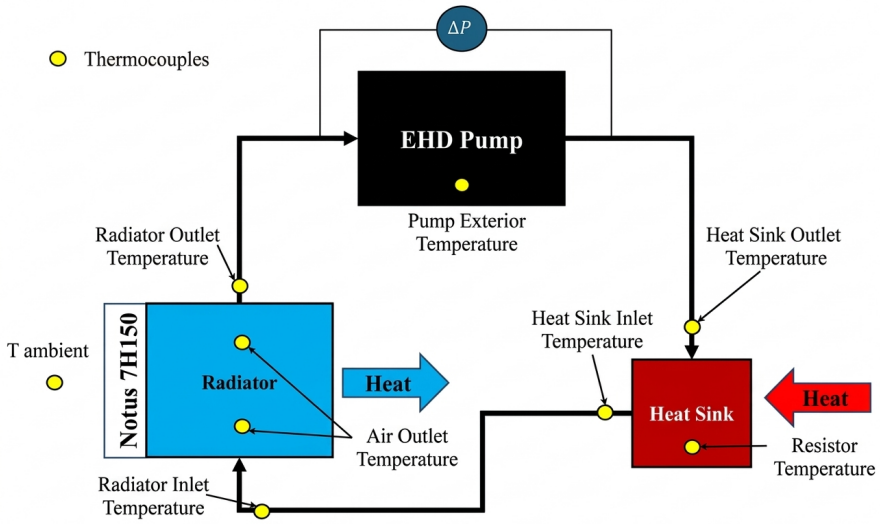


Figure 4.9: Schematic diagram showing the placement of thermocouples within the cooling loop.

Direct measurement of fluid pressure or velocity using standard electronic sensors was deemed unfeasible for this experimental setup. This limitation arises from two main factors: the potential material incompatibility between standard sensor components and the dielectric fluid, and the lack of specific data regarding the

fluid's physicochemical properties, which hinders the calibration and selection of an appropriate commercial sensor.

To address this, a U-shaped flexible silicone tube manometer containing a trapped volume of air in its upper section, was employed. This apparatus measures the pump's manometric head at both the inlet and outlet. This configuration allows for the derivation of the static pressure differential generated by the pump within the system.

Future experimental phases aim to incorporate direct fluid velocity measurements utilizing Particle Image Velocimetry (PIV) or comparable optical techniques.

4.1.4 Thermal Model

The cooling system is modeled as a closed loop comprising three main components: the EHD pump, the radiator, and the heat sink. To analyze the transient behavior of the system, a lumped-parameter thermal model is adopted. Each i-th component is treated as a thermal node characterized by a mass M_i, a specific heat C_i, and a uniform temperature T_i.

The starting point is the general energy balance equation for a control volume:

$$\frac{dE_{vc}}{dt} = \dot{m}(h_e - h_s) + \dot{Q}_{gen} - \dot{Q}_{loss} \tag{4.1}$$

Expressing the control volume energy as a function of the body's heat capacity, $E_{vc} = M_i C_i T_i$, the differential equation governing the temperature evolution of each component becomes:

$$M_i C_i \frac{dT_i}{dt} = \dot{m} C_p (T_{e,i} - T_{s,i}) + \dot{Q}_{gen} - \dot{Q}_{loss} \tag{4.2}$$

where $\dot{m}$ is the mass flow rate of the heat transfer fluid, C_p is its specific heat, and $T_{e,i}$ and $T_{s,i}$ are the fluid inlet and outlet temperatures, respectively. The term $\dot{Q}_{loss}$ represents the heat dissipation to the external environment at temperature T_{amb}, modeled as:

$$\dot{Q}_{loss} = (UA)_{loss,i} \cdot (T_i - T_{amb}) \tag{4.3}$$

To determine the fluid outlet temperature $T_{s,i}$, the internal heat exchange along the component is analyzed. Assuming the component body maintains a uniform temperature T_i, the infinitesimal energy balance for the fluid along the flow direction x can be written as:

$$\dot{m} C_p dT = hP dx (T_i - T) \tag{4.4}$$

To solve this differential equation, we define a temperature difference variable $\theta(x) = T(x) - T_i$, which implies that $d\theta = dT$. Substituting θ into the balance equation yields:

$$\dot{m} C_p \frac{d\theta}{dx} = -hP\theta \tag{4.5}$$

Separating the variables, the equation becomes:

$$\frac{1}{\theta} d\theta = -\frac{hP}{\dot{m} C_p} dx \tag{4.6}$$

The detailed analytical integration step for this temperature profile from the inlet ($x = 0$, where $\theta_o = T_{e,i} - T_i$) to the outlet ($x = L$, where $\theta_L = T_{s,i} - T_i$) is illustrated in Figure 4.10.

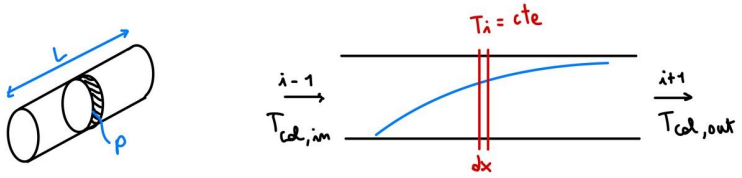


Figure 4.10: Analytical derivation and mathematical integration of the fluid temperature profile along the heat exchanger length.

Integrating both sides of the equation yields:

$$\int_{\theta_o}^{\theta_L} \frac{1}{\theta} d\theta = -\int_0^L \frac{hP}{\dot{m}C_p} dx \tag{4.7}$$

$$\ln\left(\frac{\theta_L}{\theta_o}\right) = -\frac{hPL}{\dot{m}C_p} \tag{4.8}$$

By defining the overall internal thermal conductance of the i-th component as $UA_{HX,i} = hPL$, and taking the exponential of both sides, we obtain:

$$\frac{\theta_L}{\theta_o} = e^{-\frac{UA_{HX,i}}{\dot{m}C_p}} \implies \theta_L = \theta_o e^{-\frac{UA_{HX,i}}{\dot{m}C_p}} \tag{4.9}$$

Substituting back the definitions of θ_o and θ_L yields:

$$T_{s,i} - T_i = (T_{e,i} - T_i) e^{-\frac{UA_{HX,i}}{\dot{m}C_p}} \tag{4.10}$$

$$T_{s,i} = T_i + (T_{e,i} - T_i) e^{-\frac{UA_{HX,i}}{\dot{m}C_p}} \tag{4.11}$$

It is worth noting that the overall internal thermal conductance of the components, $UA_{HX,i}$, is not a constant parameter but strongly depends on the fluid dynamic conditions. Specifically, it is a function of the mass flow rate $\dot{m}$ of the heat transfer fluid.

Assuming a forced convection heat transfer regime inside the channels (in accordance with classical empirical correlations for turbulent or transition flows, such as the Dittus-Boelter equation), the convective heat transfer coefficient varies proportionally to the mass flow rate raised to a typical exponent of 0.8. Therefore, given a baseline thermal conductance $UA_{HX}(\dot{m}_1)$ evaluated at a reference mass flow rate $\dot{m}_1$, the analytical value of the conductance for any operational mass flow rate $\dot{m}_2$ can be estimated by applying the following scaling law:

$$UA_{HX}(\dot{m}_2) = UA_{HX}(\dot{m}_1) \cdot \left(\frac{\dot{m}_2}{\dot{m}_1}\right)^{0.8} \tag{4.12}$$

During the experimental characterization phase, the system was tested under three different mass flow rate regimes. By applying Equation 4.12 starting from

the baseline operational values, the updated UA_{HX} values were determined for the main heat exchangers of the cooling loop, namely the Heat Sink and the Radiator. Conversely, for the specific assumptions of this model, the thermal conductance term relative to the EHD Pump was considered independent of the flow rate and kept constant at a value of 100.

The results of the UA_{HX} parameter adaptation as a function of the mass flow rate $\dot{m}_i$ are summarized in Table 4.2.

$\dot{\mathbf{m}}_\mathbf{i}$ **[kg/s]**	$\mathbf{UA_{HX,cal}}$ [W/K]	$\mathbf{UA_{HX,rad}}$[W/K]	$\mathbf{UA_{HX,bomba}}$[W/K]
0.0017	1	10	100
0.002125	1.195	11.954	100
0.00255	1.383	13.831	100

Table 4.2: Variation of the internal thermal conductance UA_{HX} as a function of the mass flow rate for the system components.

Finally, to allow the implementation of the model and the iterative comparison with the collected experimental data, the differential equation (4.2) is discretized in time using the Forward Euler method. Denoting the current time step with the superscript k and the subsequent one, separated by a time step Δt, with $k+1$, the update equation is obtained:

$$T_i^{k+1} = T_i^k + \frac{\Delta t}{M_i C_i}\left[\dot{m} C_p (T_{e,i}^k - T_{s,i}^k) + \dot{Q}_{gen} - (UA)_{loss,i}(T_i^k - T_{amb})\right] \tag{4.13}$$

This recursive equation allows plotting the theoretical curves for each component. The variable parameters (such as the thermal capacity $M_i C_i$, and the conductances $UA_{HX,i}$ and $(UA)_{loss,i}$) will then be calibrated to minimize the deviation from the continuous trend of the experimental data.
Based on the general discretization provided in Equations (4.11) and (4.13), the lumped-parameter thermal model is applied specifically to each of the three main components of the cooling loop. The physical connections dictate that the fluid outlet temperature of one component becomes the inlet temperature of the subsequent one.

Based on the general discretization provided in Equations (4.11) and (4.13), the lumped-parameter thermal model is applied to the entire cooling loop without particularizing the equations for each single element.

The nine characteristic parameters of the system—specifically the thermal capacity $M_i C_i$, the ambient heat loss coefficient $(UA)_{loss,i}$, and the internal thermal conductance $UA_{HX,i}$ for each component—have been fitted from the experimental data results. The complete set of these calibrated parameters is given in Table **??**.

Furthermore, the baseline mass flow rate $\dot{m}_1$ of the dielectric fluid was estimated experimentally by an energy balance in the heater (heat sink) in steady-state regime:

$$\dot{Q}_{gen} = \dot{m}_1 C_p (T_{s,cal} - T_{e,cal}) \tag{4.14}$$

Then, for different applied voltages to the electrodes, the following proportion is

assumed based on EHD scaling laws:

$$\dot{m}_2 = \dot{m}_1 \left(\frac{V_2}{V_1} \right) \tag{4.15}$$

The baseline values established for these parameters prior to the experimental calibration are detailed in Table 4.3, assuming a constant initial ambient temperature (T_{amb}) of 23.55 °C.

	cal	rad	bomb
$M_i C_i$ [J/K]	100	300	1000
$(UA)_{loss,i}$ [W/K]	0	0.0005	0.005
$UA_{HX,i}$ [W/K]	1	10	100

Table 4.3: Lumped-parameter thermal model baseline properties for the cooling loop components (evaluated at $\dot{m} = 0.0017$ kg/s).

4.2 Results and Analysis

Figure 4.11 illustrates the direct comparison between the time evolution of the experimentally measured temperatures and those simulated by the analytical model. Specifically, the body temperature of the heat sink (T_{cal}), along with the fluid temperature at its inlet (T_{cal_in}) and outlet (T_{cal_out}), are analyzed.

Rather than merely focusing on the numerical calibration, it is crucial to understand the experimental procedure that generated these thermal profiles. The measurement protocol was carefully designed to evaluate the cooling system's performance across different operating regimes. As depicted in the graph, the temperature evolution clearly exhibits distinct zones, which directly correspond to sequential step-changes in the mass flow rate of the dielectric fluid.

These varying mass flow rates were achieved by modulating the DC voltage applied to the wire electrodes of the EHD pump. The experiment began by allowing the system to heat up and reach a steady-state operation at a baseline voltage of 8 kV. Once the thermal equilibrium was established—visible as the first extended temperature plateau—the voltage was increased to 10 kV, and subsequently to 12 kV. (Further minor adjustments to 12.5 kV and 14 kV were tested near the end of the sequence).

The core of this experimental protocol consisted of testing these distinct mass flow rates and deliberately waiting for the establishment of steady-state operation at each specific step. As the applied voltage increases, the ion-drag pumping effect intensifies, delivering a higher mass flow rate. Consequently, the internal convective heat transfer is enhanced, forcing the system components and the working fluid to stabilize at progressively lower equilibrium temperatures.

(Note: In the graphs presented, the time axis has been truncated at approximately 60 minutes to isolate the physical steady-state steps. The sharp temperature

drop observed in the initial raw data after this point was not a real physical phenomenon, but rather a computational artifact of the numerical model's boundary conditions shutting down).

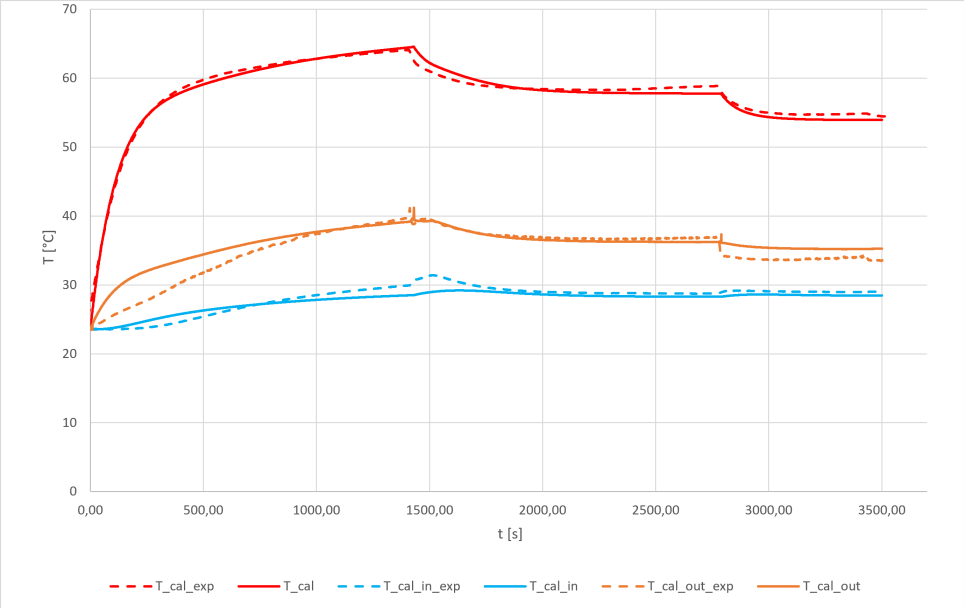


Figure 4.11: Experimental vs. numerical validation of the body and working fluid temperatures at the heat sink over time.

To achieve the high degree of agreement observed in Figure 4.11, a calibration (tuning) process was performed on the theoretical model. Specifically, the lumped parameters were iteratively refined to minimize the error between the simulated curves and the experimental data. The calibration only focused on the following variables:

- **Thermal capacity (M_iC_i):** The thermal inertia of the circuit depends on the equivalent masses of the various components (heat sink, radiator, pump). By adjusting these thermal masses in the model, it was possible to match the slopes of the temperature curves during the initial heating transient, thereby accurately replicating the physical response time of the test rig.

- **Global heat transfer coefficient ($(UA)_{loss,i}$):** To align the steady-state temperatures (the horizontal asymptotes), the thermal resistances modeling the heat dispersion to the external environment were calibrated. This parameter is crucial to account for the naturally imperfect thermal insulation of the tubing and the physical enclosures, but also especially to emulate the heat dissipation capacity of the radiator.

- **Internal thermal conductance ($UA_{HX,i}$) and Net thermal power ($\dot{Q}_{gen}$):** While $UA_{HX,i}$ was updated dynamically based on the mass flow rate, baseline values were fine-tuned to match internal convection. Additionally, the actual fraction of thermal power absorbed by the dielectric fluid ($\dot{Q}_{gen}$) compared to the nominal 30 W supplied by the electrical resistors was slightly tuned.

This ensures that the net heat in the energy balance correctly reflects the real operating conditions and accounts for parasitic losses near the heat source.

The results confirm the validity of the adopted modeling approach. The temperature difference (ΔT) between the heat sink outlet and inlet predicted by the model flawlessly replicates the one recorded by the data acquisition system. This confirms the correct estimation of both the mass flow rate ($\dot{m}$) and the specific heat capacity (C_p) of the dielectric oil (V330) used in the loop. The slight discrepancies visible during the steady-state phase—such as the minor fluctuations in the experimental curves—are perfectly expected. They can be attributed to the inherent measurement noise of the thermistors and to micro-variations of the ambient temperature in the laboratory, effects that the macroscopic analytical model naturally tends to smooth out.

Following the analysis of the thermal behavior across the heat source, the investigation focused on the heat dissipation component of the loop: the liquid-to-air radiator. To validate the predictive capabilities of the lumped-parameter thermal model for this component, the fluid temperatures at the radiator inlet (T_{rad_in}) and outlet (T_{rad_out}) were analyzed.

Figure 4.12 presents a side-by-side comparison of the experimental data and the theoretical numerical curves for both sections over the duration of the test. As established by the loop architecture, the fluid entering the radiator corresponds directly to the heated fluid exiting the CPU heat sink.

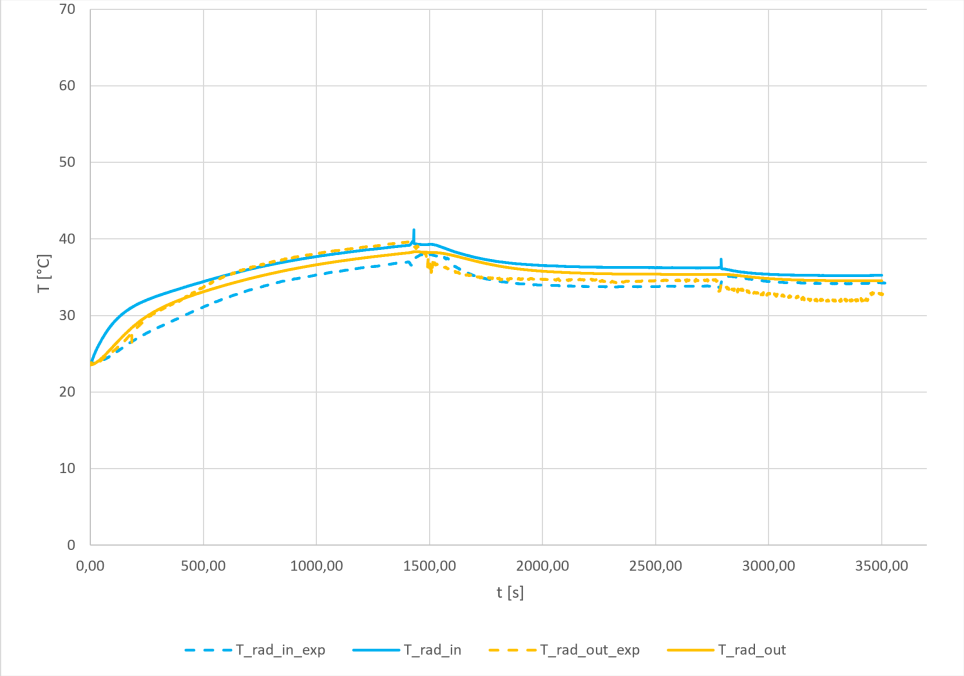


Figure 4.12: Experimental vs. numerical validation of the dielectric fluid temperature at the radiator inlet and outlet. The dashed lines represent the experimental measurements, while the solid lines depict the theoretical model.

As observed in both subplots of Figure 4.12, the lumped-parameter model demonstrates a remarkable out-of-the-box agreement with the experimental measurements.

During the first 1500 seconds, the system undergoes a classic first-order heating transient, governed by the thermal inertia ($M_i C_i$) of the components, with the inlet temperature peaking near 40°C and the outlet temperature successfully cooled to approximately 35°C by the EHD-driven airflow.

A defining feature of these thermal profiles is the presence of distinct downward step-like transitions occurring after $t = 1500$ s and $t = 2800$ s. These thermal shifts are not random fluctuations but directly correspond to the multi-step experimental protocol, during which the mass flow rate ($\dot{m}$) of the dielectric fluid was sequentially increased (as detailed in Table 3.2). According to the established scaling laws, an increase in the mass flow rate enhances the internal convective heat transfer coefficient following the relation $UA_{HX} \propto \dot{m}^{0.8}$. This reduction in internal thermal resistance forces the radiator to stabilize at progressively lower equilibrium plateaus.

The theoretical curves seamlessly track these multi-regime transitions without requiring any additional empirical tuning or forced calibration of the baseline coefficients. The minor discrepancies visible—such as slight overestimations or underestimations during the steady-state plateaus—are well within acceptable experimental margins. They can be primarily attributed to minor fluctuations in the laboratory ambient temperature and the intrinsic measurement tolerance of the thermocouples. Overall, the accurate reproduction of both the initial transient slope and the subsequent steady-state plateaus validates the 1D thermal resistance network as a reliable tool for characterizing the cooling capacity of the EHD-assisted radiator.

The final component analyzed within the lumped capacitance thermal model is the EHD ion-drag pump. To assess the accuracy and predictive capability of the numerical code for this specific device, the computed transient temperature was compared against experimental data. The experimental benchmark was obtained from the thermocouple measuring the external casing temperature of the prototype.

The calibration of the lumped parameter model for the pump required a coordinated tuning of two primary physical properties that govern the system's thermodynamics: the total thermal capacity ($M \cdot C_p$) and the overall heat transfer coefficient for ambient losses (UA_{loss}).

During the initial calibration stages, adjusting the transient response was critical to replicating the thermal inertia of the physical bench. Consequently, the lumped thermal mass parameter of the pump was calibrated and set to $M \cdot C_p = 1200$ J/K. As illustrated in Figure 4.13, this tuning allowed the model's transient curve to closely follow the experimental slope during the first minutes of operation, showcasing an excellent agreement in terms of thermal response time.

Regarding the steady-state regime, which is governed by convective environmental losses via the UA_{loss} parameter, the calibration process highlighted a classic compromise inherent to lumped parameter modeling. Setting the ambient loss coefficient to $UA_{loss} = 0.005$ W/K allows the analytical code to predict the working fluid temperatures throughout the entire closed loop with remarkable precision, particularly matching the experimental curves of the heater inlet temperature (T_{cal_in}). However, this fluid-optimized setup leads to an overestimation of the pump's nodal temperature, which asymptotes at approximately 30°C compared to the 27.6°C recorded experimentally in the steady-state phase.

This discrepancy is fully justifiable from a thermodynamic perspective. The

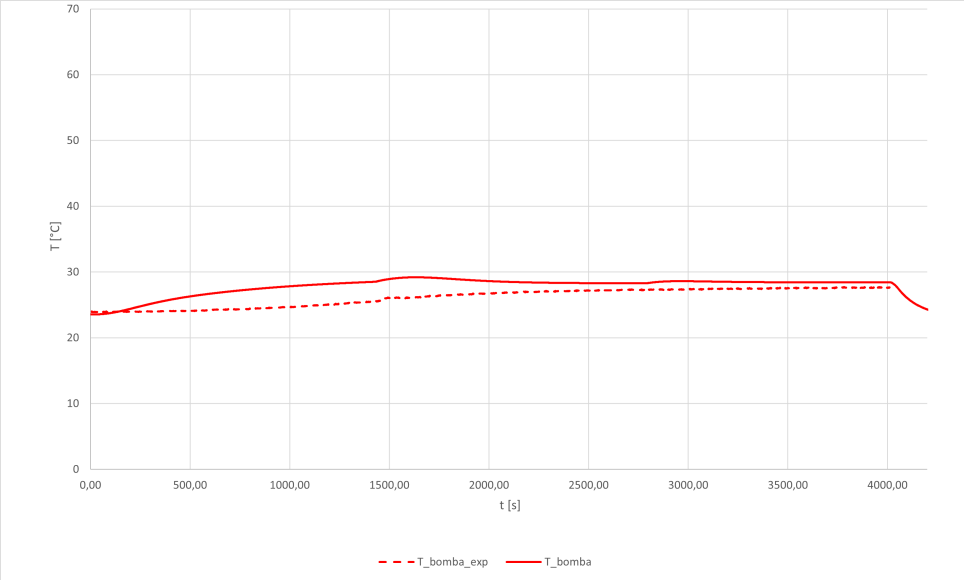


Figure 4.13: Comparison between experimental data and simulated temperature of the ion-drag pump during the transient heating phase ($M \cdot C_p = 1200$ J/K, $UA_{loss} = 0.005$ W/K).

mathematical model simplifies the component into a single homogenous thermal node, thus calculating a bulk (average) temperature heavily influenced by the internal core where the hot fluid flows (~ 30°C). Conversely, the experimental sensor captures a localized surface temperature on the outer casing, which is naturally colder due to direct convective dissipation to the ambient air (25.1°C).

Since the primary objective of this thermal model is to ensure an accurate prediction of the thermodynamic state of the dielectric fluid—a critical variable governing electrohydrodynamic pumping performance—priority was given to the loop's fluid temperatures. Therefore, maintaining $UA_{loss} = 0.005$ W/K represents the most robust engineering compromise, accepting the minor and physically sound deviation at the pump casing to preserve absolute accuracy across the fluid domain.

Chapter 5

PIV Flow Characterization

5.1 PIV Characterization Setup

Particle Image Velocimetry (PIV) [22][1], a non-intrusive optical velocimetry method, was employed to analyze the fluid flow velocity field at the pump outlet. This technique entails seeding the fluid with tracer particles, illuminating them with a planar laser sheet, and recording their positions in consecutive frames to determine particle displacement via cross-correlation algorithms.

5.1.1 Challenges in EHD Applications

The application of PIV in Electrohydrodynamic (EHD) pumps introduces specific challenges due to the presence of intense electric fields. These fields exert electrical forces on the tracer particles. If these forces are comparable to or exceed the hydrodynamic drag of the fluid, the particles may fail to accurately follow the flow streamlines [18]. Consequently, tracer selection is critical and must prioritize minimizing electrical interactions.

To mitigate these effects, particles must possess a low tendency to acquire surface charge—reducing the Coulomb force [10] and a low electrical permittivity to limit the dielectrophoretic (DEP) force arising from the dielectric mismatch at the fluid-particle interface. It is noted, however, that the DEP force is generally negligible compared to the Coulomb force [10][9].

The migration velocity (U_{mig}), defined as the difference between the particle velocity and the fluid velocity, can be estimated by balancing the Stokes drag force on the particle with the Coulomb force:

$$3\pi\mu_f d_p U_{mig} = F_{e,p} \tag{5.1}$$

Where $F_{e,p} \approx q_p E$. Assuming the particle reaches the saturation charge calculated by Pauthenier [12] as $q_p = 3\pi\epsilon d_p^2 E$, the balance equation leads to:

$$U_{mig} \leq \frac{\epsilon d_p}{\mu_f} E^2 \tag{5.2}$$

In the vicinity of the pump outlet, where PIV measurements are conducted, the electric field is significantly weaker than in the inter-electrode region. Consequently,

the migration velocity is estimated to be $U_{mig} \approx 5$ mm/s at 20 kV, and significantly lower at reduced voltages, scaling with E^2 while fluid velocity scales with E.

5.1.2 Tracer Particle Selection

To prevent sedimentation or migration toward the free surface, tracers must possess a density comparable to that of the fluid. Furthermore, they require a low Stokes number (Stk) to minimize particle inertia and accurately track flow variations. To ensure high-fidelity flow tracking, Stk must be significantly less than unity. The Stokes number is defined as the ratio of the particle relaxation time (τ_p) to the characteristic flow time scale (τ_f):

$$Stk = \frac{\tau_p}{\tau_f} = \frac{\rho_p d_p^2 U}{18 \mu L} \tag{5.3}$$

Where:

- ρ_p and d_p are the particle density and diameter, respectively.
- μ is the dynamic viscosity of the fluid.
- U and L are the characteristic velocity and length scales of the flow.

A design trade-off exists: while a low Stk ensures streamline adherence, particles must be sufficiently large to scatter enough light for the imaging system. For these velocimetry tests, the fluid was seeded with 30 μm diameter hollow glass spheres ($\rho_p = 600$ kg/m^3). This electrically neutral material allows for density tuning to match the working fluid, ensuring accurate tracking ($Stk < 0.01$ for all operating conditions) while providing sufficient scattering intensity.

5.1.3 FlowMaster Software Calculation Principles

The processing of the PIV (Particle Image Velocimetry) images acquired during the experiment was performed using the dedicated FlowMaster software [14]. The following sections briefly describe the algorithmic analysis process that leads to the generation of velocity fields from the raw images.

The first step of the analysis consists of dividing the acquired image pairs (usually referred to as Frame A and Frame B) into small square sub-areas called *Interrogation Windows*. The basic principle of the algorithm assumes that all tracer particles within a single window move homogeneously, i.e., with the same velocity and in the same direction.

To calculate the particle displacement, the software applies a mathematical procedure known as *Cross-Correlation*. The algorithm compares the group of particles within a specific window in Frame A with the corresponding area in Frame B.

The result of this statistical operation is a three-dimensional "correlation plane": the highest point of this plane, defined as the *Correlation Peak*, represents the most probable average spatial displacement of the particles. Knowing this displacement in pixels and the time delay Δt set between the two laser pulses, the software can calculate the exact velocity vector for that specific area.

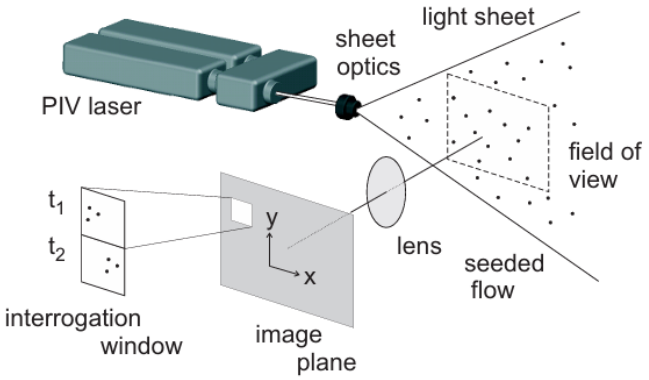


Figure 5.1: Schematic of the PIV image division into interrogation windows

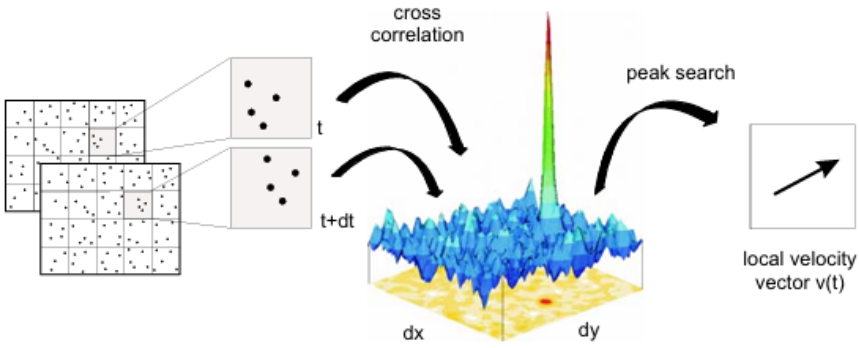


Figure 5.2: Representation of the cross-correlation peak used to identify the dominant displacement.

To significantly increase the accuracy and spatial resolution of the final vector field, the calculation is not performed in a single, simple pass, but through the combined use of two advanced techniques:

- **Overlap:** Adjacent interrogation windows are overlapped (typically by 50%). This strategy allows for extracting a larger number of vectors from the image without having to excessively reduce the size of the single window, thus ensuring a strong signal and dampening background noise.
- **Multi-pass (Iterative passes):** The analysis is repeated sequentially, progressively decreasing the window size (for example, starting from a coarse grid of 64×64 pixels and then dropping to 32×32 pixels). The coarse vector calculated during the first pass acts as an "initial estimate" to guide the correlation search in the subsequent pass with the smaller window. This approach drastically reduces erroneous vectors (spurious vectors) and increases the local reliability of the flow field.
- **Image deformation:** This technique is applied to reduce velocity gradients inside the interrogation window, drastically enhancing the accuracy of the cross-correlation.

5.1.4 Experimental Setup and Processing

The experimental setup, illustrated in Figure 5.4, was designed to provide optical access directly to the internal region of the pump, specifically between the electrodes. Images were captured from a top-down perspective using a 3.1 MPix CMOS camera (Model DMK 37BUX25). For each experimental run, 300 images were recorded at a frequency of 30 frames per second (fps).

A 1 mm thick continuous laser sheet ($\lambda = 515\ nm$) was utilized to illuminate a vertical plane near the geometric center, perpendicular to the collector planes. The measurement domain was entirely located inside the pump (i.e., in the inter-electrode gap between the tungsten wire emitter and the multiplane collector), accurately capturing the fluid flow acceleration.

Specifically, the measurement domain was located inside the pump (i.e., between the emitter and collector electrodes), capturing the fluid flow. Video sequences were recorded at various voltage levels to analyze the velocity field evolution under different pumping regimes. Image processing was performed using LaVision GmbH Davis 7 software. The analysis employed a multi-pass cross-correlation algorithm (reducing interrogation window sizes from 64×64 to 8×8 pixels) with image deformation to compute instantaneous two-dimensional velocity fields. Iterative filters were applied between passes to detect and remove outliers [18]. Finally, the average velocity and RMS magnitude were computed from the ensemble of 300 individual flow fields.

To manipulate, interpolate, and extract macroscopic kinetic metrics from these two-dimensional velocity matrices, a custom MATLAB script was developed. This post-processing step is fundamental to define the coordinate system and the directional properties of the EHD jet. Within the reference frame of the captured optical

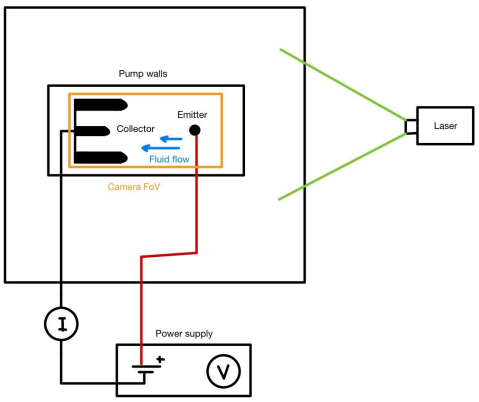


Figure 5.3: Experimental setup sketch

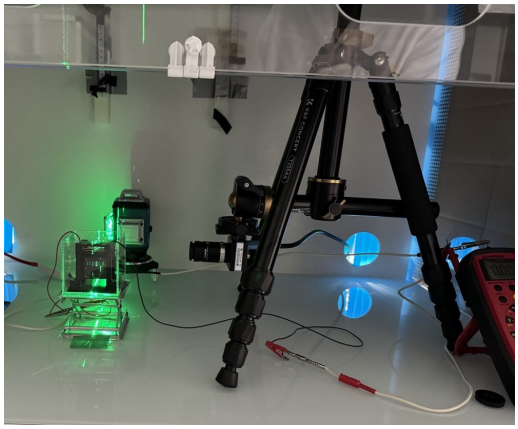


Figure 5.4: Experimental setup in the laboratory, showing the camera, the laser source, and the EHD prototype

domain, the dielectric fluid flow moves strictly from right to left, entering the window from the high-voltage emitter region and accelerating through the narrow passages of the multiplane collector.

Figure 5.5 illustrates a representative example of the reconstructed two-dimensional velocity field generated by the MATLAB script, specifically referring to Video 22 (corresponding to an applied voltage of 4000 V), where the baseline 0° configuration is applied (i.e., with the camera and laser sheet aligned directly with the mid-plane of the flow channel).

From each of these processed vector maps, two primary kinematic parameters were systematically isolated to allow for the multi-fluid comparison detailed in Chapter 4:

- **Maximum axial velocity (V_{max}):** Obtained by evaluating the velocity matrix to compute the absolute spatial peak at the core of the EHD jet. To prevent isolated spurious vectors—such as optical artifacts from laser reflections on the emitter wire or localized dielectrophoretic particle drifting—from artificially distorting the measurement, a specific Region of Interest (ROI) was defined to isolate the stable jet area. The MATLAB expression `max(max(U))` was then applied exclusively to this masked domain, ensuring the extracted maximum represents the true physical fluid momentum.

- **Average axial velocity (V_{media}):** To evaluate the velocity profile and extract specific local values, a two-dimensional bilinear interpolation was performed on the regular PIV grid using the MATLAB `interp2` function. Due to the different optical access and reference frames associated with the camera tilt angles, two distinct axial target positions were selected for the data extraction. Specifically, an axial target of $x = -8$ mm was defined for the 0° camera configuration, whereas an axial target of $x = -2$ mm was used for the 30° configuration. For both cases, the local velocity values were extracted at two symmetric transverse positions located at $y = 1.5$ mm (v_{up}) and $y = -1.5$ mm (v_{down}).

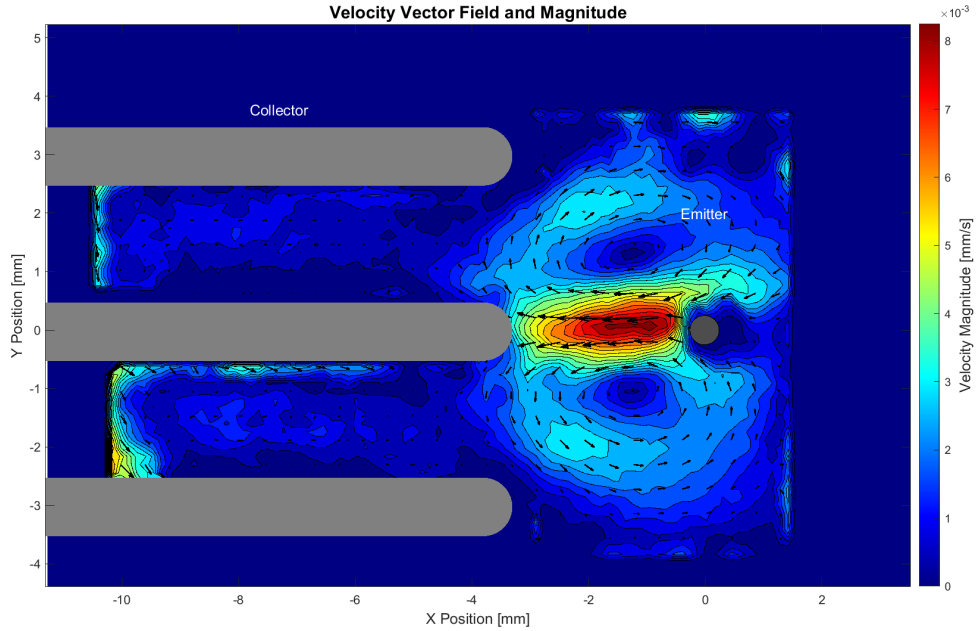


Figure 5.5: Representative example of the time-averaged two-dimensional velocity field processed via the custom MATLAB script (corresponding to Video 22 at 4000 V, baseline 0° configuration). The vector field and contour levels clearly demonstrate that the fluid flow propagates from right to left, with the superimposed emitter and multiplane collector geometry highlighting the EHD acceleration region and the lateral recirculation zones.

5.2 Results and Analysis

5.2.1 Flow Topology and Secondary Structures

To visually corroborate the presence of three-dimensional structures and evaluate the actual flow topology generated by the ion-drag pump, this section presents the processed PIV velocity vector fields. The images analyzed herein correspond to the central symmetry plane (the 0° baseline configuration) to isolate the core momentum transfer and minimize lateral wall boundary effects.

Figure 5.6 illustrates the flow fields for three representative applied voltages: 2000 V, 3500 V, and 5000 V. As the applied voltage increases, the main electrohydrodynamic jet becomes distinctly visible. This "electric wind" strongly accelerates the dielectric fluid from the emitter wire straight through the center of the multiplane collector.

Simultaneously, the intense momentum transfer from this high-velocity central jet to the surrounding stationary fluid induces the formation of two prominent lateral recirculation zones (upper and lower vortices). These secondary structures grow in spatial extension and kinetic energy proportionally with the applied voltage. As will be discussed in the subsequent quantitative analysis, a significant portion of the injected electrical power is continuously dissipated to sustain these large-scale swirling motions, ultimately limiting the net forward axial velocity.

While Figure 5.5 illustrates the global velocity magnitude including transverse

secondary flows, Figure 5.6 isolates the axial velocity component (U). This isolation is required for a rigorous comparison with the 1D theoretical model (Equation 3.8), which strictly predicts the axial momentum transfer.

5.2.2 Maximum Velocity Characterization

To further characterize the kinematic performance of the ion-drag pump using OLEON as the dielectric fluid, a detailed analysis of the flow velocity field was conducted. This section presents the comparison between the maximum axial velocity (V_{max}) extracted from the experimental PIV measurements and the corresponding theoretical predictions. To ensure physical accuracy and prevent algorithmic errors, the `max(max(U))` matrix search was not applied globally across the entire field of view independently of the flow location. Instead, it was strictly confined to a predefined spatial Region of Interest (ROI) centered precisely on the actual location of the EHD jet core. This geographic bounding guarantees that the extracted maximums correspond strictly to the true convective fluid momentum and not to isolated spurious vectors located outside the primary flow path. The experimental dataset analyzed herein compares two optical configurations: the baseline case with the camera aligned at 0° relative to the main flow plane, and an inclined setup at 30°. The fundamental difference between these two measurement configurations lies in the optical alignment relative to the internal electrodes.

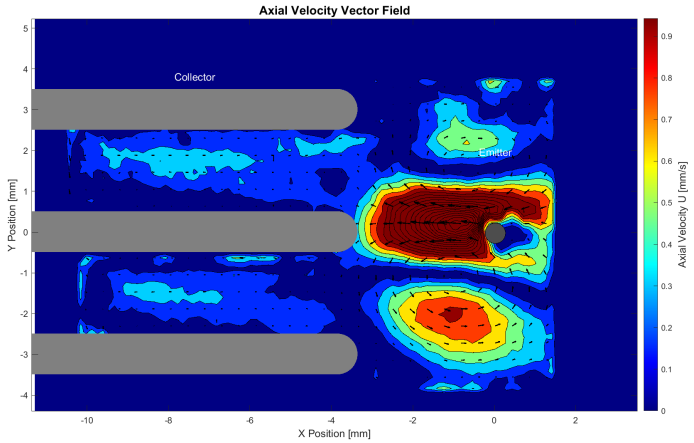
The 0° baseline configuration aligns the image axis of the field of view directly with the central plane of the ground electrode. Conversely, the 30° inclined setup is intentionally designed to obtain a clear line of sight to the emitting wire. By tilting the image axis, it becomes possible to visually access the wire, distinguishing the flow dynamics without being strictly constrained to the central plane of the collector.

As detailed in the experimental logs (Appendix B, Table B.5), specific voltage levels (namely 3000 V and 3500 V) were sampled at multiple recording frequencies and exposure times (Δt). For these overlapping data points, the velocity matrices derived from the videos with the shortest exposure times (highest framerates) were strictly selected for the quantitative analysis. A longer exposure time in PIV inherently acts as a temporal low-pass filter; it temporally averages the particle displacements across velocity gradients, artificially dampening the true instantaneous spatial peaks of the EHD jet. Therefore, selecting the shortest available Δt ensures the most accurate and unattenuated representation of the maximum fluid velocity.

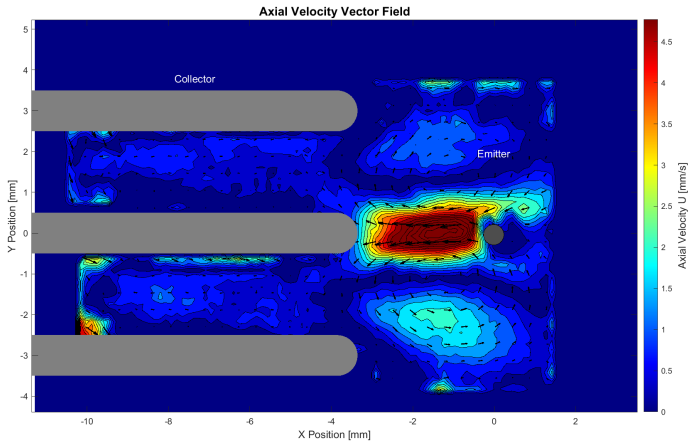
To generate the theoretical curves for the maximum velocity presented in Figure 5.7, the baseline thermodynamic parameters ($V_{SCL} = 1500$ V and charge injection efficiency $\eta = 0.3$) were kept constant, as derived from the global multi-variable regression that will be detailed in Section 5.2.4. Therefore, the analytical model was fitted to the experimental V_{max} data points purely by manually calibrating an empirical linear scaling factor (k_{loss}), representing the hydrodynamic kinetic energy losses.

Figure 5.7 illustrates these experimental data points alongside the analytical curves derived from the one-dimensional electrohydrodynamic (EHD) flow model.

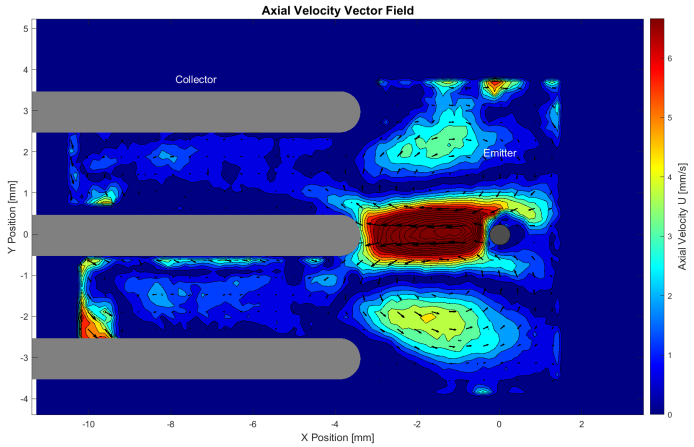
Before analyzing the theoretical trends, it is important to address an apparent



(a) Applied Voltage: 2000 V



(b) Applied Voltage: 3500 V



(c) Applied Voltage: 5000 V

Figure 5.6: Evolution of the time-averaged axial velocity component (U) at the 0° central plane. The sequence isolates the development of the main EHD jet along the primary pumping direction as the applied voltage increases, providing the quantitative basis for the validation of the 1D analytical model.

visual discrepancy between the maximum velocities reported in Figure 5.7 (peaking at approximately 6.8 mm/s at 5000 V) and the absolute maximums visible in the color bars of the 2D contour plots in Figure 5.6 (which suggest localized peaks up to 12 mm/s). The raw spatial peak derived from the `max(max(U))` expression often captures isolated, spurious high-velocity vectors located immediately adjacent to the emitter wire. These localized artifacts are caused by intense laser reflections on the metallic tungsten surface and strong dielectrophoretic particle drifting near the corona discharge. For the quantitative analysis in Figure 5.7, these near-electrode optical artifacts were deliberately filtered out via the previously mentioned ROI, to correctly plot the true physical peak velocity of the stable EHD jet.

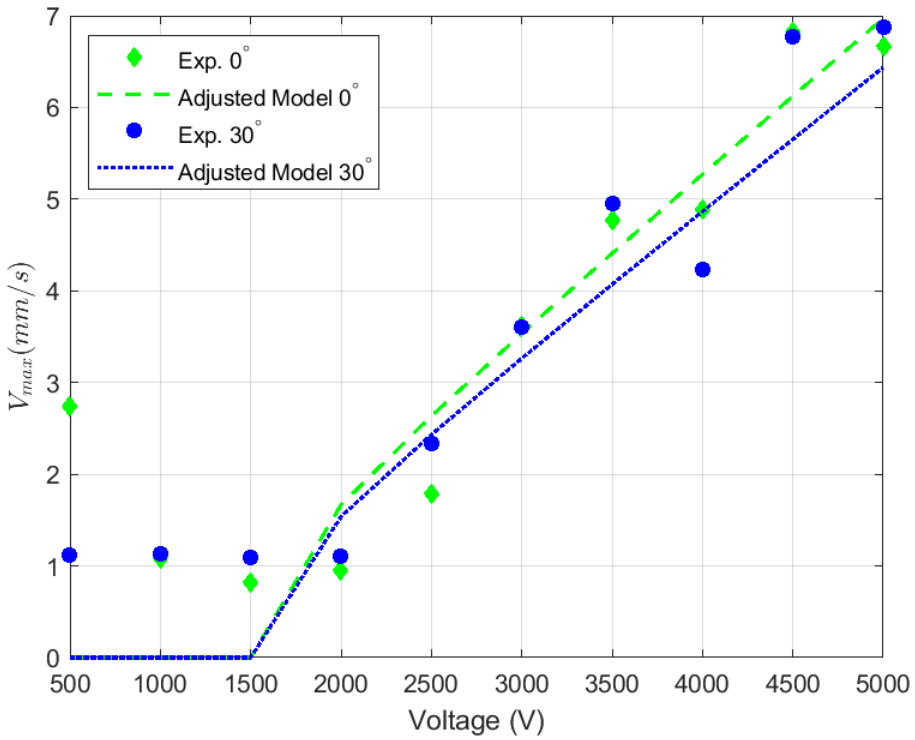


Figure 5.7: Maximum axial velocity (V_{max}) as a function of the applied DC voltage for the OLEON fluid. The experimentally measured PIV data points (markers) for 0° and 30° camera tilts are compared against the adjusted theoretical 1D EHD models ($V_{max,adjusted}$, lines).

As observed in Figure 5.7, while the theoretical models successfully capture the scaling trend of the experimental velocity for applied voltages above 2500 V, their raw ideal magnitudes heavily overestimate the physical measurements. Furthermore, it is important to clarify that the experimental maximum velocity does not exhibit a quadratic growth; instead, it transitions into a distinct quasi-linear trend at higher operating voltages. This behavior is perfectly consistent with the underlying EHD transport theory. While the electrostatic Coulomb force and the resulting body force pressure scale quadratically with the voltage ($\Delta P \propto V(V - V_{SCL})$), the localized fluid velocity is proportional to the square root of this pressure drop ($V_{max} \propto \sqrt{\Delta P}$). Consequently, this square-root dependency counteracts the quadratic scaling of the electric field, resulting in the linearized velocity progression observed in the higher

voltage regimes. To reconcile the simplified 1D analytical framework with the real-world data, an empirical hydrodynamic efficiency factor (k_{loss}) was explicitly introduced into the equations. This coefficient acts as a direct linear multiplier applied to the theoretical maximum velocity ($V_{max,adjusted} = k_{loss} \cdot V_{max,1D}$) to globally account for the 3D viscous dissipation and internal flow resistance. The resulting $V_{max,adjusted}$ values, computed directly in mm/s, are the ones represented in Figure 5.7 alongside the experimental measurements.Specifically, a factor of $k_{loss} = 0.76$ was applied to the 0° configuration, and $k_{loss} = 0.70$ to the 30° configuration. These scaling factors indicate an effective kinetic energy conversion of 76% and 70% at the core of the EHD jet relative to the ideal lossless case. While the core momentum remains highly efficient, the necessity for these calibrations stems from fundamental discrepancies between the simplified 1D theory and the actual physical system:

- **Idealized Jet Velocity vs. Actual Momentum Transfer**: The simplified empirical model provides an order of magnitude for the velocity of the jet (v^*) arising directly between the emitting wire and the grounded electrode. For this precise reason, the PIV post-processing routine was designed to extract the local spatial maximum situated at the core of the EHD jet to ensure a direct and consistent comparison. However, the theoretical equation inherently assumes a perfectly ideal, frictionless, and one-dimensional momentum transfer. This idealized assumption inevitably overestimates the true physical velocity of the jet, which is subjected to drag and interaction with the surrounding stagnant fluid.

- **Hydrodynamic Restrictions and Viscous Dissipation:** The multiplane collector geometry acts as a major physical obstruction, introducing substantial local hydraulic resistance that restricts fluid acceleration and induces significant viscous dissipation within the narrow channels.

- **Three-Dimensional Flow Structures:** As qualitatively evidenced by the PIV velocity vectors presented in Section 5.2.1, a meaningful portion of the injected electrical energy is dissipated to sustain complex, three-dimensional secondary flows, such as lateral recirculation zones. Because these multi-dimensional effects do not contribute to the macroscopic forward axial velocity, they constitute the primary physical justification for treating the simplified 1D framework not as a predictive analytical model, but strictly as a behavioral scaling law.

Notably, the V_{max} data points for the 0° and 30° planes are remarkably close in magnitude across the voltage sweep. Unlike the average flow velocity, which is highly sensitive to the boundary layer proximity in the 30° slice, the localized peak search algorithm successfully captures the core of the EHD jet in both optical planes, resulting in minimal deviation between the two setups.

Lastly, a fundamental physical and methodological distinction must be made regarding the lowest testing voltages (500 V, 1000 V, and 1500 V). At these sub-threshold conditions ($V_0 \leq V_{SCL}$), the applied voltage is insufficient to initiate charge injection; consequently, a macroscopic EHD jet is absent, and the true convective

fluid velocity is physically zero. However, Figure 5.7 displays non-zero maximum velocities in this regime. Specifically, the apparent peak at 500 V (reaching approximately 2.74 mm/s for the 0° configuration) represents a clear contradiction. Rather than indicating a local convective flow, this specific point is a numerical artifact of the PIV cross-correlation algorithm, which misinterprets intense localized laser reflections on the emitter wire or structural micro-vibrations as a residual velocity vector. Similarly, the stable plateau of approximately 1 mm/s observed at 1000 V and 1500 V across both optical configurations represents the intrinsic background noise floor (or minimum velocity resolution limit) of the PIV software under zero-flow regimes. In these static conditions, minor parasitic effects—including localized dielectrophoretic particle drifting—are computed as a baseline residual field, which must be interpreted strictly as the lower measurement boundary of the current experimental setup rather than actual EHD transport.

5.2.3 Experimental Extraction of the flow-rate

To evaluate the practical pumping capacity of the device, it is necessary to estimate its macroscopic volumetric flow rate. This requires transitioning from the localized velocity maps obtained via Particle Image Velocimetry (PIV) to a representative average axial velocity (V_{media}). Following the experimental characterization, the flow within the multiplane collector is channeled into parallel rectangular passages. Assuming a fully developed laminar flow between parallel plates—governed by the classical Poiseuille flow solution—the velocity profile across the channel gap takes a parabolic shape. Analytically, the mean velocity (V_m) in a parabolic profile is strictly related to the maximum centerline velocity (V_{cl}) by the geometric ratio:

$$V_m = \frac{2}{3} V_{\mathrm{cl}} \tag{5.4}$$

In the post-processing routine, the spatial coordinates for extracting the velocity profiles were selected via visual inspection of the time-averaged PIV velocity contours (previously presented in Figure 5.6). The local velocity extraction was implemented using the `interp2` command instead of a scattered data interpolator like `griddata`. Since the PIV post-processing generates data on a rectilinear and uniformly spaced mesh, the use of `interp2` ensures a more precise and computationally efficient bilinear interpolation, avoiding potential smoothing artifacts typical of scattered data algorithms. As visually summarized in Figure 5.8, the chosen cross-sections represent a core region where the fluid jet is symmetric, stable, and minimally affected by outlet boundary layer expansion or external aerodynamic disturbances. The extracted upper and lower velocities, converted into mm/s by multiplying the MATLAB output by a factor of 1000, provide a reliable estimation of the local flow behavior under the applied electric field. The overall experimental average velocity was then computed by averaging the centerline velocities of both channels and scaling them by the Poiseuille flow factor:

$$V_{\mathrm{media,\ exp}} = \frac{2}{3} \left(\frac{v_{\mathrm{up}} + v_{\mathrm{down}}}{2} \right) \tag{5.5}$$

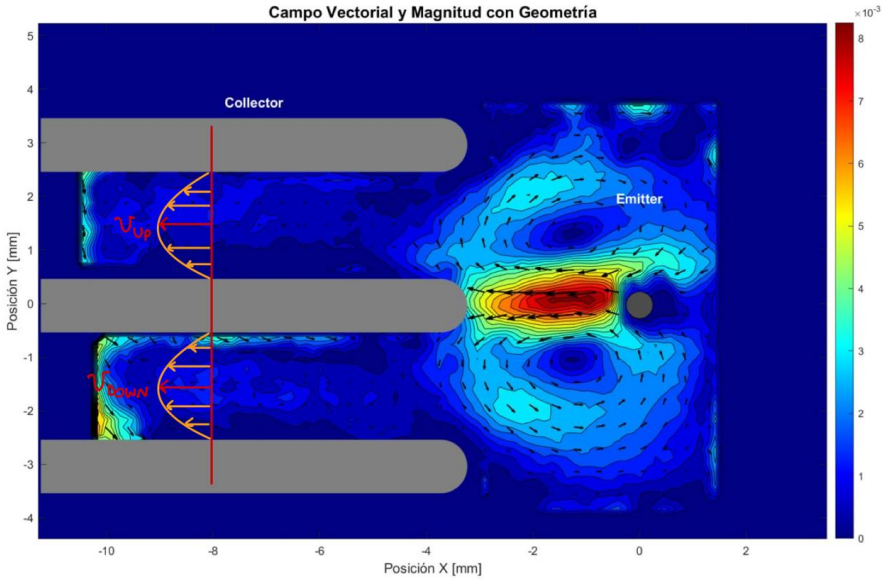


Figure 5.8: Schematic representation of the velocity profile extraction at $x = -8$ mm. The superimposed parabolic curves illustrate the assumed fully developed Poiseuille flow within the upper (v_{up}) and lower (v_{down}) collector channels.

5.2.4 Comparison with the Analytical Model

The experimental average velocities extracted for both the baseline configuration (0° central plane) and the inclined configuration (30° off-center plane) were compared against the one-dimensional analytical electrohydrodynamic (EHD) model developed in Section 3.1.4. To ensure physical alignment with the local measurements inside the collector channels, the theoretical bulk velocity was scaled by the geometric area ratio ($Geo_Factor = A_{\text{Ref}}/A_{\text{Canal}}$), accounting for the restriction from the 1 mm thick collector plates.

Figure 5.9 illustrates the direct comparison between the experimental data points and the continuous theoretical trends as a function of the applied DC voltage.

As observed in Figure 5.9, the analytical curves replicate the physical threshold behavior of the pump.

The theoretical models were calibrated to the experimental data utilizing a custom multi-variable regression MATLAB script presented in Listing A.1. This numerical routine performs a simultaneous fitting of the three characteristic experimental curves: the consumed electrical current (V-I), the generated static pressure head (V-H), and the macroscopic fluid velocity (V-V_{max}). By minimizing the normalized squared differences across these three domains simultaneously, the space-charge-limited threshold voltage (V_{SCL}) and the charge injection efficiency (η) were accurately determined for each dielectric medium. The extracted parameters for the three fluids are summarized in Table 5.1.

Below this strict cut-in voltage, the macroscopic EHD jet is not initiated. The microscopic, non-zero velocity magnitudes extracted at 500 V and 1000 V do not represent bulk fluid transport, but are rather attributed to algorithmic cross-correlation noise and local dielectrophoretic particle drifting. Above the 1500 V threshold, the

Table 5.1: Extracted threshold voltage (V_{SCL}) and charge injection efficiency (η) for the tested dielectric fluids.

Fluid	V_{SCL} *(kV)*	η *(-)*
V330	1.0	0.90
CUTMAX	2.5	0.60
OLEON	1.5	0.30

velocity growth is proportional to $\sqrt{V_0(V_0 - V_{SCL})}$. While this relation introduces a slight non-linear curvature immediately after the cut-in threshold, it rapidly transitions into a strictly linear regime at higher applied voltages (where $V_0 \gg V_{SCL}$), accurately capturing the steady macroscopic momentum transfer from the accelerated ions to the neutral fluid.

To achieve precise agreement with the experimental datasets, the analytical framework was tuned by introducing an empirical hydrodynamic loss coefficient (k_{loss}). Consistent with the maximum velocity analysis, this factor is applied as a direct linear multiplier to the theoretical bulk velocity ($V_{\text{media, adjusted}} = k_{\text{loss}} \cdot V_{\text{media, 1D}}$) to globally account for the unmodeled viscous drag and multi-dimensional flow losses. The calibrated values for each optical setup are:

- **Baseline Configuration (0°):** $k_{\text{loss}} = 0.15$
- **Inclined Configuration (30°):** $k_{\text{loss}} = 0.10$

To properly map the analytical 1D EHD theoretical framework to the experimental PIV velocity fields, an empirical hydrodynamic efficiency coefficient, denoted as k_{loss}, must be introduced. The analytical 1D model inherently assumes an ideal, uniform convective motion. However, the real pump geometry presents severe structural restrictions. To ensure rigorous geometric consistency across all the analyzed fluids (Nycobase V330, Cutmax, and Oleon), the macroscopic channel cross-section ($A_{canal} = 0.022 \times 0.04$ m^2) is uniformly applied as the reference scaling area for the theoretical models.

Following this geometric standardization, the calibration for the Oleon fluid yields a k_{loss} of approximately 0.76 for the maximum velocity model and 0.15 for the average bulk velocity model. These values provide a solid physical interpretation of the internal flow dynamics. The maximum velocity coefficient indicates that the central EHD jet core is highly efficient, conserving about 76% of its ideal kinetic momentum.

However, as experimentally mapped via PIV, the structural boundaries of the manifold plates induce massive 3D recirculation zones. These secondary flow patterns, which are topologically characteristic of the Notus-3P geometry and occur consistently across different dielectric fluids, act as a severe momentum sink for the bulk fluid transport. Consequently, the global hydrodynamic efficiency of the average mass transport drops to 15% ($k_{loss} = 0.15$). This significant differential between the maximum and average k_{loss} accurately models the kinetic energy dissipation caused by the massive recirculation, reconciling the theoretical predictions with the

observed kinematic order of magnitude without underestimating the performance of the core EHD jet.

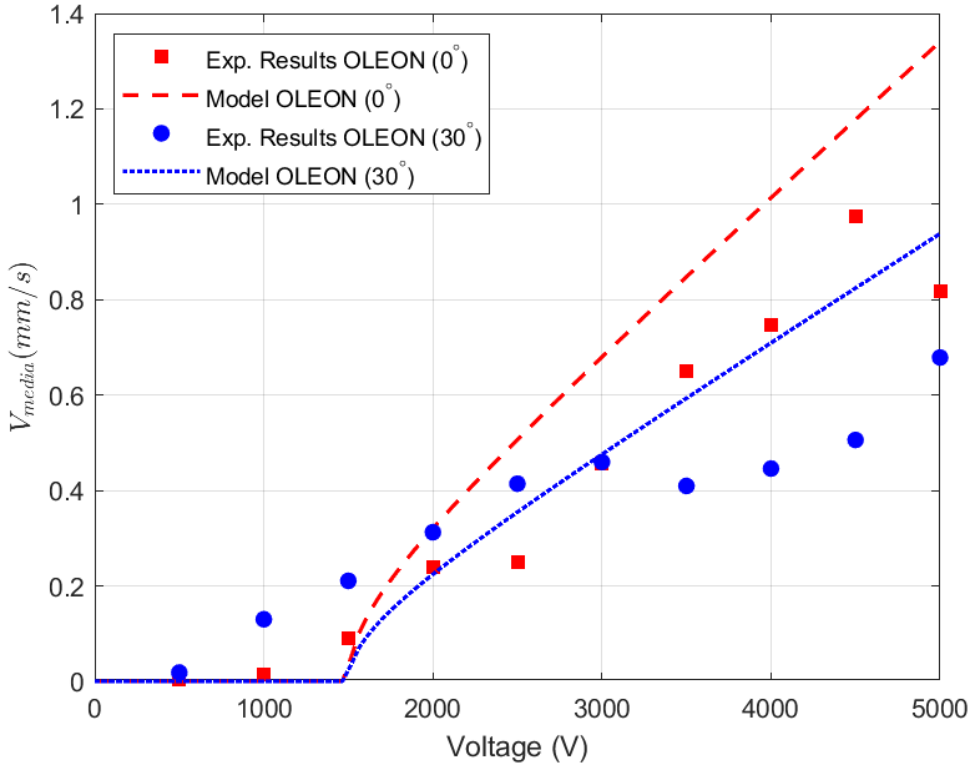


Figure 5.9: Experimental average axial velocity (V_{media}) for the OLEON fluid at 0° and 30° camera tilts compared against the calibrated theoretical 1D EHD model.

Crucially, Figure 5.9 reveals that the average velocities recorded at a 30° camera tilt are systematically lower than those at 0°, a discrepancy that highlights the three-dimensional nature of the flow. While the 0° plane captures the centerline velocity profile where fluid momentum is at its peak, the 30° inclined plane samples a diagonal slice that approaches the lateral solid walls of the rectangular duct. Due to the no-slip boundary condition, the fluid velocity naturally decays near all physical boundaries. Consequently, the local hydrodynamic efficiency drops, requiring a lower calibration factor ($k_{\text{loss}} = 0.007$) to capture the enhanced viscous dampening experienced near the channel walls. Furthermore, beyond the physical hydrodynamic dampening, the optical measurement parameters must be considered when comparing the two configurations. As detailed in Appendix B (Table B.5), the recording frame rate (fps) and the exposure time, corresponding to the time between images (tbi), were dynamically adjusted from 30 fps (tbi = 33.33 ms) at lower voltages up to 180 fps (tbi = 5.56 ms) at 5000 V. While these adjustments were applied symmetrically to both the 0° and 30° optical setups to properly track the increasing EHD jet momentum, the finite exposure time inherently acts as a temporal low-pass filter. In regions characterized by complex three-dimensional velocity gradients, such as the 30° inclined plane, this temporal averaging can further dampen the instantaneous particle displacements computed by the cross-correlation algorithm. Consequently, the experimental setup itself contributes to the lower

macroscopic average velocity observed in the off-center measurements.

5.2.5 Multi-Fluid Kinematic Comparison

To provide a comprehensive evaluation of the pump's kinematic performance across different dielectric mediums, a global comparison was reconstructed. Figure 5.10 illustrates the average fluid velocity as a function of the applied DC voltage, contrasting the theoretical one-dimensional (1D) models with the experimental datasets for the V330, CUTMAX, and OLEON fluids.

For the OLEON fluid, the experimental data points represent the macroscopic bulk velocity derived from the PIV measurements at the 0° central plane. These values were calculated by applying the Poiseuille parabolic profile approximation to the centerline channel velocities and subsequently converted to cm/s to ensure dimensional consistency with the historical datasets of V330 and CUTMAX.

As depicted in Figure 5.10, the experimental results for V330 and CUTMAX follow their respective uncalibrated 1D theoretical scaling laws with acceptable margins. Conversely, the OLEON data points exhibit a severe downward discrepancy, remaining significantly below the ideal 1D model predictions across the entire voltage sweep. This kinematic behavior highlights that for highly viscous fluids operating within restrictive and compact collector geometries, a parameter regression fitted exclusively on static pressure and current is fundamentally insufficient to capture the true fluid dynamic field.

The massive kinetic energy dissipation caused by multi-dimensional secondary structures, high viscous drag, and local recirculation zones—qualitatively evidenced in the preceding PIV vector fields—provides the explicit physical justification for this deviation. Consequently, these findings establish the necessity of introducing strict hydrodynamic calibration factors (k_{loss}) to reconcile the idealized analytical models with the actual behavior of the pump.

5.2.6 Volumetric Flow Rate Estimation

Based on the macroscopic experimental average axial velocity (V_{media}) characterized in Section 4.3.3, the total volumetric flow rate (Q) generated by the ion-drag pump can be directly quantified. Evaluating the volumetric displacement is essential to judge the pump's operational capability for localized fluid circulation and cooling applications.

The total volumetric flow rate is analytically defined as the product of the mean fluid velocity and the total cross-sectional area orthogonal to the flow direction (A_{total}). Due to the specific wire-multiplane architecture of the Notus-3P prototype, the counter-electrode consists of three parallel metallic plates that partition the primary flow into two identical, parallel rectangular channels. Consequently, the total effective area available for fluid discharge is exactly twice the cross-section of a single passage ($A_{total} = 2 \cdot A_{canal}$). The governing equation is expressed as follows:

$$Q = V_{media} \cdot A_{total} = 2 \cdot V_{media} \cdot A_{canal} \tag{5.6}$$

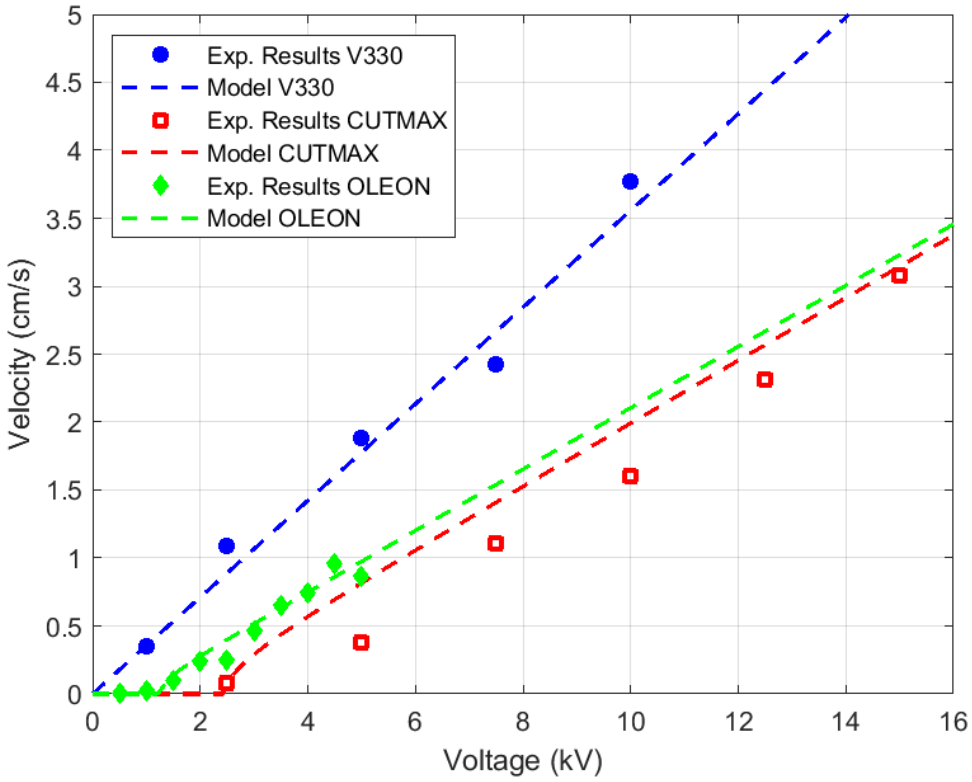


Figure 5.10: Comparison of the fluid velocity as a function of the applied DC voltage for V330, CUTMAX, and OLEON. The plot highlights the severe discrepancy between the ideal 1D analytical model and the experimental PIV data for the OLEON fluid, indicating the presence of dominant three-dimensional hydrodynamic losses.

where $A_{canal} = h \cdot w$ represents the cross-sectional area of a single channel, determined by the plate spacing ($h = 2$ mm) and the effective channel width ($w = 30$ mm).

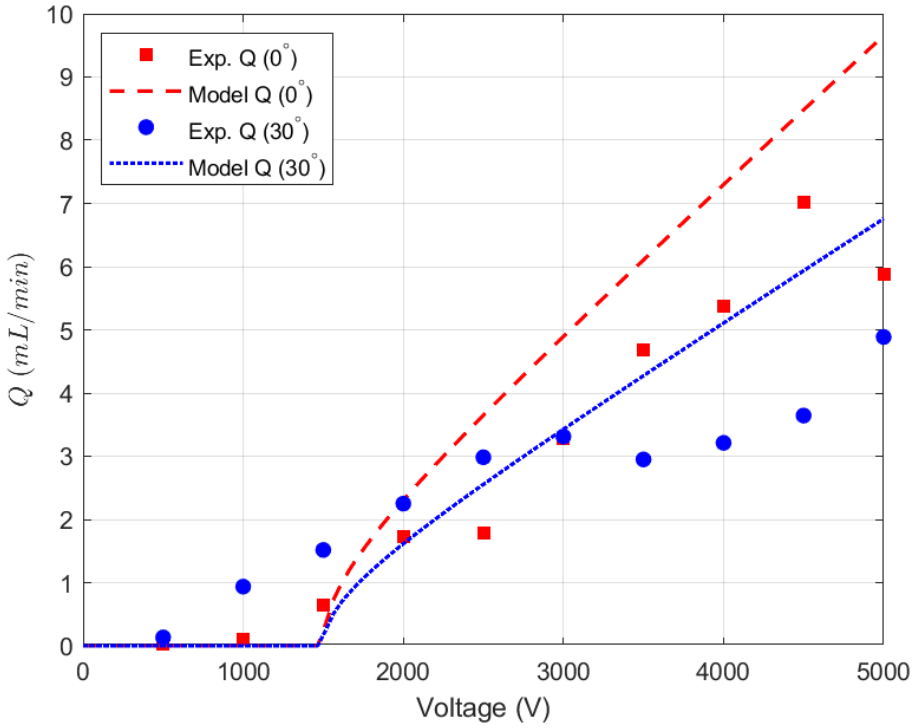


Figure 5.11: Estimated volumetric flow rate (Q) as a function of the applied DC voltage. The experimental data and calibrated 1D EHD theoretical models are compared for the 0° and 30° optical configurations.

Figure 5.11 illustrates the volumetric flow rate as a function of the applied voltage. Since the flow rate is a linear geometric scaling of the average velocity, Q directly inherits the non-linear, threshold-governed quadratic behavior observed in the previous kinematic analysis. Below the characteristic cut-in voltage of $V_{SCL} = 1500$ V, the flow rate remains identically zero as no charge injection occurs. Above this operational threshold, the flow rate exhibits a progressive parabolic growth.

At the highest testing potentials (4500 V - 5000 V), the theoretical model predicts a volumetric flow rate approaching 9.5 mL/min for the core flow (0°), while the experimental data indicates a peak output in the range of 6 to 7 mL/min. It is crucial to emphasize that the true volumetric flow rate is a global macroscopic property of the system; therefore, the physical flow rate generated at a given voltage must be identical regardless of the optical measurement plane. The apparent discrepancy—where the Q estimated from the 30° off-center plane is systematically lower (peaking around 5 mL/min) than that derived from the 0° central plane—is an artifact of the extrapolation method and lack of spatial calibration. Because the 30° plane captures a localized region with lower velocities due to viscous dampening near the lateral walls, estimating the total bulk flow directly from this single 2D slice without a dedicated 3D spatial integration factor inherently underestimates the global volumetric output.

While this standalone flow rate characterizes the hydrodynamic capacity of a single EHD stage under static optical testing conditions, it provides a crucial quantitative benchmark for evaluating the feasibility of the pump in heat transfer loops, validating future multi-stage configurations, and tuning numerical multi-physics computational fluid dynamics (CFD) models.

Chapter 6

Conclusion

The primary objective of this thesis was the comprehensive experimental characterization and analytical modeling of the Notus-3P wire-multiplane ion-drag pump prototype. Through a structured evaluation encompassing electro-hydraulic performance, thermal management integration, and kinematic flow analysis, this research bridged the gap between idealized one-dimensional theoretical scaling laws and the complex physical behavior of electrohydrodynamic devices.

The electro-hydraulic characterization demonstrated that both the generated static pressure and the consumed electrical current scale quadratically with the applied DC voltage, confirming the fundamental momentum transfer mechanisms of EHD ion-drag pumping. Across the evaluated dielectric fluids, V330 exhibited superior performance, driven by a high relative permittivity and an optimal charge injection efficiency. In contrast, the OLEON fluid presented a lower injection efficiency, yet maintained the expected physical threshold behaviors.

The practical cooling capacity of the prototype was successfully validated by integrating the pump into a hybrid air-liquid thermal loop. A custom lumped-parameter thermal network model accurately captured both the initial heating transients and the steady-state equilibrium plateaus of the system. The precise alignment between the numerical predictions and the experimental temperature profiles confirmed that the analytical thermal resistance network is a highly reliable tool for predicting the thermodynamics of the EHD-assisted radiator under varying mass flow rates.

However, the kinematic flow analysis conducted via Particle Image Velocimetry (PIV) revealed critical limitations in applying simplified one-dimensional fluid dynamic models to compact EHD geometries. The optical measurements of the highly viscous OLEON fluid uncovered complex, three-dimensional secondary structures, including prominent lateral recirculation zones. These vortices, combined with the severe viscous drag imposed by the narrow multiplane passages, dissipate a significant portion of the kinetic energy. Consequently, the classical theoretical scaling laws vastly overestimated the true convective fluid momentum. To reconcile these discrepancies, specific hydrodynamic calibration factors were introduced, highlighting that the actual kinetic energy conversion is substantially lower than ideal frictionless assumptions.

Ultimately, this research validates the capability of the wire-multiplane EHD geometry to function as an effective, silent, solid-state fluid driver for advanced cooling

applications. The findings emphasize that future advancements in ion-drag pump design must strictly account for multi-dimensional flow interactions and prioritize the optimization of internal hydraulic profiles to minimize viscous dissipation.

Appendix A

Matlab Code Snippets

```
% ================================================================
% PROGRAMA PARA GRAFICAR DATOS EXPERIMENTALES FRENTE A MODELO IVP
% CON REGRESIÓN DE PARÁMETROS (V_SCL y eta) PARA V330, CUTMAX Y
    OLEON
% ================================================================

%% Limpieza del Entorno
clear; clc; close all;

%% 1. ENTRADA DE DATOS EXPERIMENTALES
% ----------------------------------------------------------------
V_IP_exp = 0:1:20; % Vector de Tensión para Intensidad/Presión (kV)

% --- NYCOBASE (Fluido 1) ---
I_exp1 = [0, 0.04, 0.09, 0.16, 0.22, 0.29, 0.36, 0.43, 0.5, 0.57,
    0.64, 0.71, 0.78, 0.87, 0.97, 1.05, 1.15, 1.24, 1.39, 1.56,
    1.79];
P_exp1 = [0, 0, 0, 16.87, 25.31, 42.18, 50.62, 75.93, 92.80,
    109.68, 134.99, 160.30, 177.17, 210.92, 261.53, 295.28, 354.34,
    413.39, 464.01, 539.94, 599.00];
V_vel_exp1 = [1, 2.5, 5, 7.5, 10];
v_exp1 = [0.3545, 1.0917, 1.8841, 2.4227, 3.767];

% --- CUTMAX (Fluido 2) ---
I_exp2 = [0, 0.01, 0.02, 0.02, 0.03, 0.04, 0.05, 0.06, 0.08, 0.1,
    0.12, 0.14, 0.16, 0.19, 0.22, 0.26, 0.3, 0.35, 0.42, 0.57,
    0.67];
P_exp2 = [0, 0, 0, 0, 0, 0, 7.65, 15.30, 15.30, 15.30, 22.96,
    30.61, 38.26, 53.56, 61.21, 76.52, 91.82, 107.13, 130.08,
    168.34, 191.30];
V_vel_exp2 = [2.5, 5, 7.5, 10, 12.5, 15];
v_exp2 = [0.0835, 0.3757, 1.108, 1.6071, 2.312, 3.0841];

% --- OLEON (Fluido 3) ---
I_ofset_exp3=0.03;
I_exp3 = [0.03, 0.05, 0.06, 0.07, 0.09, 0.11, 0.13, 0.14, 0.15,
    0.17, 0.20, 0.22, 0.26, 0.29, 0.33, 0.37, 0.42, 0.47, 0.52,
    0.60, 0.62]-I_ofset_exp3;
P_exp3 = [0.00, 0.00, 7.93, 15.86, 15.86, 15.86, 23.79, 23.79,
    31.72, 31.72, 39.65, 39.65, 47.58, 55.51, 71.37, 79.30, 95.16,
```

```
    111.02, 118.95, 142.74, 158.61];
% Nota: de-comentado para que el fminsearch tenga datos.
V_vel_exp3 = [0.5, 1.0, 1.5, 2.0, 2.5, 3.0, 3.5, 4.0, 4.5, 5.0];
v_exp3 = [0.0024, 0.0199, 0.0956, 0.2381, 0.2479, 0.4616, 0.6486,
    0.7405, 0.9596, 0.8658];

%% 2. PARÁMETROS FÍSICOS
% -------------------------------------------------------------------
epsilon_0 = 8.854e-12;
AREA_Ref = 0.003 * 0.025;   % Área de referencia experimental
AREA_Canal = 0.022 * 0.04;  % Área del canal
GAP_NT = 0.004;             % Distancia entre electrodos (m)
Geo_Factor = (AREA_Ref / AREA_Canal) * 100; % *100 para cm/s

% --- Propiedades NYCOBASE ---
epsilon_NY = 3.2;
sigma_NY = 1.445e-11;
rho_NY = 860;
mu_NY = 3.06e-3;
K_NY = 2e-11 / mu_NY;
K_H_NY = 1.815e-7;
NY_base = sqrt(epsilon_NY * epsilon_0 / rho_NY);

% --- Propiedades CUTMAX ---
epsilon_CUT = 2.0;
Sigma_CUT = 1.82e-15;
rho_CUT = 780;
mu_CUT = 2.52e-3;
K_CUT = 2e-11 / mu_CUT;
K_H_CUT = 1.507e-7;
CUT_base = sqrt(epsilon_CUT * epsilon_0 / rho_CUT);

% --- Propiedades OLEON ---
epsilon_OLEON = 3.2;
Sigma_OLEON = 1.44e-11;
rho_OLEON = 808;
mu_OLEON = 7.5e-3;
K_OLEON = 2e-11 / mu_OLEON;
K_H_OLEON = 1.82e-7;
OLEON_base = sqrt(epsilon_OLEON * epsilon_0 / rho_OLEON);

%% 3. REGRESIÓN DE PARÁMETROS (V_SCL y eta)
% -------------------------------------------------------------------
disp('Calculando regresiones... por favor espera.');

% Opciones para la optimización
options = optimset('Display', 'off', 'TolFun', 1e-6, 'TolX', 1e-6);

% Función anónima para NYCOBASE [p(1) = V_SCL en kV, p(2) = eta]
obj_NY = @(p) calc_error(p, V_IP_exp, I_exp1, P_exp1, V_vel_exp1,
    v_exp1, ...
                         epsilon_NY, sigma_NY, K_NY, K_H_NY,
                            NY_base, GAP_NT, AREA_Ref, Geo_Factor,
                            epsilon_0);
p0_NY = [1.0, 0.9];
p_opt_NY = fminsearch(obj_NY, p0_NY, options);
```

```
V_SCL_NY = p_opt_NY(1) * 1000;
eta_NY   = p_opt_NY(2);

% Función anónima para CUTMAX [p(1) = V_SCL en kV, p(2) = eta]
obj_CUT = @(p) calc_error(p, V_IP_exp, I_exp2, P_exp2, V_vel_exp2, v_exp2, ...
                          epsilon_CUT, Sigma_CUT, K_CUT, K_H_CUT, CUT_base, GAP_NT, AREA_Ref, Geo_Factor, epsilon_0);
p0_CUT = [2.5, 0.6];
p_opt_CUT = fminsearch(obj_CUT, p0_CUT, options);
V_SCL_CUT = p_opt_CUT(1) * 1000;
eta_CUT   = p_opt_CUT(2);

% --- Regresión para el OLEON ---
obj_OLEON = @(p) calc_error(p, V_IP_exp, I_exp3, P_exp3, V_vel_exp3, v_exp3, ...
                            epsilon_OLEON, Sigma_OLEON, K_OLEON, K_H_OLEON, OLEON_base, GAP_NT, AREA_Ref, Geo_Factor, epsilon_0);
p0_OLEON = [1.5, 0.7]; % Valores iniciales de prueba para [V_SCL, eta]
p_opt_OLEON = fminsearch(obj_OLEON, p0_OLEON, options);
V_SCL_OLEON = p_opt_OLEON(1) * 1000; % Guarda la tensión de inicio óptima (en V)
eta_OLEON   = p_opt_OLEON(2);        % Guarda la eficiencia óptima

disp('Regresiones completadas');

%% 4. CÁLCULO DE MODELOS CON LOS PARÁMETROS OPTIMIZADOS
% ---------------------------------------------------------------------
V_mod_kV = linspace(0, 20, 100);
V_mod = V_mod_kV * 1000;
V_mod_safe = max(V_mod, eps); % Previene la división por cero

% Para NYCOBASE
V_diff_NY = V_mod - V_SCL_NY;
V_diff_NY(V_diff_NY < 0) = 0;
V_eff_sq_NY = V_mod .* V_diff_NY;
P_model_NY = eta_NY * epsilon_NY * epsilon_0 * V_eff_sq_NY / (GAP_NT^2);
I_inj_NY = (eta_NY * epsilon_NY * epsilon_0 .* V_eff_sq_NY / (GAP_NT^3)) .* (K_NY + K_H_NY .* sqrt(eta_NY .* V_diff_NY ./ V_mod_safe));
I_ohm_NY = sigma_NY * V_mod / GAP_NT;
I_model_NY = (I_inj_NY + I_ohm_NY) * AREA_Ref * 1e6; % uA
v_model_NY = (sqrt(eta_NY .* V_diff_NY ./ V_mod_safe) .* (K_H_NY .* V_mod / GAP_NT)) * Geo_Factor;

% Para CUTMAX
V_diff_CUT = V_mod - V_SCL_CUT;
V_diff_CUT(V_diff_CUT < 0) = 0;
V_eff_sq_CUT = V_mod .* V_diff_CUT;
P_model_CUT = eta_CUT * epsilon_CUT * epsilon_0 * V_eff_sq_CUT / (GAP_NT^2);
```

```
I_inj_CUT = (eta_CUT * epsilon_CUT * epsilon_0 .* V_eff_sq_CUT / (GAP_NT^3)) .* (K_CUT + K_H_CUT .* sqrt(eta_CUT .* V_diff_CUT ./ V_mod_safe));
I_ohm_CUT = Sigma_CUT * V_mod / GAP_NT;
I_model_CUT = (I_inj_CUT + I_ohm_CUT) * AREA_Ref * 1e6; % uA
v_model_CUT = (sqrt(eta_CUT .* V_diff_CUT ./ V_mod_safe) .* (K_H_CUT .* V_mod / GAP_NT)) * Geo_Factor;

% Para OLEON
V_diff_OLEON = V_mod - V_SCL_OLEON;
V_diff_OLEON(V_diff_OLEON < 0) = 0;
V_eff_sq_OLEON = V_mod .* V_diff_OLEON;
P_model_OLEON = eta_OLEON * epsilon_OLEON * epsilon_0 * V_eff_sq_OLEON / (GAP_NT^2);
I_inj_OLEON = (eta_OLEON * epsilon_OLEON * epsilon_0 .* V_eff_sq_OLEON / (GAP_NT^3)) .* (K_OLEON + K_H_OLEON .* sqrt(eta_OLEON .* V_diff_OLEON ./ V_mod_safe));
I_ohm_OLEON = Sigma_OLEON * V_mod / GAP_NT;
I_model_OLEON = (I_inj_OLEON + I_ohm_OLEON) * AREA_Ref * 1e6; % uA
v_model_OLEON = (sqrt(eta_OLEON .* V_diff_OLEON ./ V_mod_safe) .* (K_H_OLEON .* V_mod / GAP_NT)) * Geo_Factor;

%% 5. GRAFICACIÓN
% ------------------------------------------------------------------
% --- Propagación de Errores ---
delta_I = 0.01;       % Error en medida de Intensidad (μA)
delta_P_NY = 8.44;    % Error en medida de Presión V330 (rho*g)
delta_P_CUT = 7.46;   % Error en medida de Presión CUTMAX (rho*g)
delta_P_OLEON = 8.00; % Estimación para OLEON

% Error propagado para Intensidad
vec_err_I1 = 0.1 * ones(size(I_exp1));
vec_err_I1(I_exp1 > 0) = 0.5 * delta_I ./ sqrt(I_exp1(I_exp1 > 0));

vec_err_I2 = 0.1 * ones(size(I_exp2));
vec_err_I2(I_exp2 > 0) = 0.5 * delta_I ./ sqrt(I_exp2(I_exp2 > 0));

vec_err_I3 = 0.1 * ones(size(I_exp3));
vec_err_I3(I_exp3 > 0) = 0.5 * delta_I ./ sqrt(I_exp3(I_exp3 > 0));

% Error propagado para Presión
vec_err_P_NY_vec = 2.9 * ones(size(P_exp1));
vec_err_P_NY_vec(P_exp1 > 0) = 0.5 * delta_P_NY ./ sqrt(P_exp1(P_exp1 > 0));

vec_err_P_CUT_vec = 2.73 * ones(size(P_exp2));
vec_err_P_CUT_vec(P_exp2 > 0) = 0.5 * delta_P_CUT ./ sqrt(P_exp2(P_exp2 > 0));

vec_err_P_OLEON_vec = 2.8 * ones(size(P_exp3));
vec_err_P_OLEON_vec(P_exp3 > 0) = 0.5 * delta_P_OLEON ./ sqrt(P_exp3(P_exp3 > 0));

% --- FIGURA 1: Raíz de Intensidad ---
figure(1); hold on;
```

```
errorbar(V_IP_exp, sqrt(I_exp1), vec_err_I1, 'b', 'LineStyle', '
    none', 'HandleVisibility', 'off');
errorbar(V_IP_exp, sqrt(I_exp2), vec_err_I2, 'r', 'LineStyle', '
    none', 'HandleVisibility', 'off');
errorbar(V_IP_exp, sqrt(I_exp3), vec_err_I3, 'g', 'LineStyle', '
    none', 'HandleVisibility', 'off');

plot(V_IP_exp, sqrt(I_exp1), 'bo', 'MarkerFaceColor', 'b', '
    DisplayName', 'Exp. Results V330');
plot(V_mod_kV, sqrt(I_model_NY), 'b--', 'LineWidth', 1.5, '
    DisplayName', 'Model V330');
plot(V_IP_exp, sqrt(I_exp2), 'rs', 'LineWidth', 2, 'DisplayName', '
    Exp. Results CUTMAX');
plot(V_mod_kV, sqrt(I_model_CUT), 'r--', 'LineWidth', 1.5, '
    DisplayName', 'Model CUTMAX');
plot(V_IP_exp, sqrt(I_exp3), 'gd', 'MarkerFaceColor', 'g', '
    DisplayName', 'Exp. Results OLEON');
plot(V_mod_kV, sqrt(I_model_OLEON), 'g--', 'LineWidth', 1.5, '
    DisplayName', 'Model OLEON');

ylim([0 1.4]);
ylabel('$\sqrt{Current}$ ($\mu A^{1/2}$)', 'Interpreter', 'latex');
xlabel('Voltage (kV)');
legend('Location', 'northwest'); grid on; box on; xlim([0 20]);
    hold off;

% --- FIGURA 2: Raíz de Presión ---
figure(2); hold on;
errorbar(V_IP_exp, sqrt(P_exp1), vec_err_P_NY_vec, 'b', 'LineStyle'
    , 'none', 'HandleVisibility', 'off');
errorbar(V_IP_exp, sqrt(P_exp2), vec_err_P_CUT_vec, 'r', 'LineStyle
    ', 'none', 'HandleVisibility', 'off');
errorbar(V_IP_exp, sqrt(P_exp3), vec_err_P_OLEON_vec, 'g', '
    LineStyle', 'none', 'HandleVisibility', 'off');

plot(V_IP_exp, sqrt(P_exp1), 'bo', 'MarkerFaceColor', 'b', '
    DisplayName', 'Exp. Results V330');
plot(V_mod_kV, sqrt(P_model_NY), 'b--', 'LineWidth', 1.5, '
    DisplayName', 'Model V330');
plot(V_IP_exp, sqrt(P_exp2), 'rs', 'LineWidth', 2, 'DisplayName', '
    Exp. Results CUTMAX');
plot(V_mod_kV, sqrt(P_model_CUT), 'r--', 'LineWidth', 1.5, '
    DisplayName', 'Model CUTMAX');
plot(V_IP_exp, sqrt(P_exp3), 'gd', 'MarkerFaceColor', 'g', '
    DisplayName', 'Exp. Results OLEON');
plot(V_mod_kV, sqrt(P_model_OLEON), 'g--', 'LineWidth', 1.5, '
    DisplayName', 'Model OLEON');

ylim([0 25]);
ylabel('$\sqrt{Pressure}$ ($Pa^{1/2}$)', 'Interpreter', 'latex');
xlabel('Voltage (kV)');
legend('Location', 'northwest'); grid on; box on; xlim([0 20]);
    hold off;

% --- FIGURA 3: Velocidad ---
figure(3); hold on;
```

```
plot(V_vel_exp1, v_exp1, 'bo', 'MarkerFaceColor', 'b', 'DisplayName', 'Exp. Results V330');
plot(V_mod_kV, v_model_NY, 'b--', 'LineWidth', 1.5, 'DisplayName', 'Model V330');
plot(V_vel_exp2, v_exp2, 'rs','LineWidth', 2, 'DisplayName', 'Exp. Results CUTMAX');
plot(V_mod_kV, v_model_CUT, 'r--', 'LineWidth', 1.5, 'DisplayName', 'Model CUTMAX');
plot(V_vel_exp3, v_exp3, 'gd', 'MarkerFaceColor', 'g', 'DisplayName', 'Exp. Results OLEON');
plot(V_mod_kV, v_model_OLEON, 'g--', 'LineWidth', 1.5, 'DisplayName', 'Model OLEON');

ylabel('Velocity (cm/s)');
xlabel('Voltage (kV)');
xlim([0 16]);
ylim([0 5]);
legend('Location', 'northwest'); grid on; box on; hold off;

% --- FIGURA 4: Resumen de Valores Calculados ---
figure(4);
axes('Position', [0 0 1 1], 'Visible', 'off');
text_res = sprintf(['\\bf{Resultados de la Regresion Lineal Normalizada}\\rm\n\n' ...
                '\\bfFluido 1: NYCOBASE (V330)\\rm\n' ...
                '   • V_{SCL} Calculado : %.2f V\n' ...
                '   • \\eta Calculado  : %.4f\n\n' ...
                '\\bfFluido 2: CUTMAX\\rm\n' ...
                '   • V_{SCL} Calculado : %.2f V\n' ...
                '   • \\eta Calculado  : %.4f\n\n' ...
                '\\bfFluido 3: OLEON\\rm\n' ...
                '   • V_{SCL} Calculado : %.2f V\n' ...
                '   • \\eta Calculado  : %.4f'], ...
                V_SCL_NY, eta_NY, V_SCL_CUT, eta_CUT, V_SCL_OLEON, eta_OLEON);
text(0.1, 0.5, text_res, 'FontSize', 12, 'Interpreter', 'tex');

%% ================================================================
% FUNCIÓN DE ERROR PARA OPTIMIZACIÓN
% ================================================================
function total_err = calc_error(p, V_IP_exp, I_exp, P_exp, V_vel_exp, v_exp, ...
                                epsilon_fluid, sigma_fluid, K_fluid, K_H_fluid, base_vel, ...
                                GAP_NT, AREA_Ref, Geo_Factor, epsilon_0)

    V_SCL = p(1) * 1000; % Convertir kV a V
    eta = p(2);

    % Penalización para mantener valores físicos
    if V_SCL < 0 || eta < 0
        total_err = 1e6;
        return;
    end

```

```
    % --- Evaluar modelo en puntos experimentales ---
    V_ip_V = V_IP_exp * 1000;
    V_vel_V = V_vel_exp * 1000;

    % Valores seguros para evitar división por cero
    V_ip_safe = max(V_ip_V, eps);
    V_vel_safe = max(V_vel_V, eps);

    % Para P e I
    V_diff_ip = V_ip_V - V_SCL;
    V_diff_ip(V_diff_ip < 0) = 0;
    V_eff_sq_ip = V_ip_V .* V_diff_ip;

    P_mod = eta * epsilon_fluid * epsilon_0 * V_eff_sq_ip / (GAP_NT
        ^2);
    I_inj = (eta * epsilon_fluid * epsilon_0 .* V_eff_sq_ip / (
        GAP_NT^3)) .* (K_fluid + K_H_fluid .* sqrt(eta .* V_diff_ip
        ./ V_ip_safe));
    I_ohm = sigma_fluid * V_ip_V / GAP_NT;
    I_mod = (I_inj + I_ohm) * AREA_Ref * 1e6;

    % Para v
    V_diff_vel = V_vel_V - V_SCL;
    V_diff_vel(V_diff_vel < 0) = 0;

    v_mod = (sqrt(eta .* V_diff_vel ./ V_vel_safe) .* (K_H_fluid .*
         V_vel_V / GAP_NT)) * Geo_Factor;

    % --- Cálculo de Errores Normalizados (Least Squares) ---
    norm_I = sum(((sqrt(I_mod) - sqrt(I_exp)) ./ max(sqrt(I_exp)))
        .^2);

    valid_P = sqrt(P_exp) >= 2;
    if any(valid_P)
         norm_P = sum(((sqrt(P_mod(valid_P)) - sqrt(P_exp(valid_P)))
             ./ max(sqrt(P_exp(valid_P)))).^2);
    else
         norm_P = 0;
    end

    norm_v = sum(((v_mod - v_exp) ./ max(v_exp)).^2);

    % Error total
    total_err = norm_I + norm_P + norm_v;
end
```

Listing A.1: Pressure experiment code

```
clear
close all
clc

%% 1. MODELO DE VELOCIDAD MAXIMA
V_mod_max = [500, 1000, 1500, 2000, 2500, 3000, 3000, 3500, 3500,
    4000, 4500, 5000];
v_x_max_exp_0 = [2.7380, 1.0750, 0.8150, 0.9430, 1.7840, 2.1230,
```

```
    3.6160, 2.7740, 4.7720, 4.8870, 6.8260, 6.6690];
v_x_max_exp_30 = [1.1200, 1.1310, 1.0970, 1.1111, 2.3290, 2.4960,
    3.6050, 3.4670, 4.9530, 4.2270, 6.7700, 6.8810];

epsilon_0 = 8.854e-12;
AREA_Ref = 0.003 * 0.025;
AREA_Canal = 0.022 * 0.04;
GAP_NT = 0.004;
Geo_Factor = AREA_Ref / AREA_Canal;
V_SCL_OLEON = 1.5 * 1000;
eta_OLEON = 0.3;

k_loss_0 = 0.763;
k_loss_30 = 0.704;

epsilon_OLEON = 3.2;
rho_OLEON = 808;
OLEON_base = sqrt(epsilon_OLEON * epsilon_0 / rho_OLEON);

V_diff_OLEON_max = V_mod_max - V_SCL_OLEON;
V_diff_OLEON_max(V_diff_OLEON_max < 0) = 0;
V_eff_sq_OLEON_max = V_mod_max .* V_diff_OLEON_max;

v_avg_model = sqrt(eta_OLEON) * (OLEON_base * sqrt(
    V_eff_sq_OLEON_max) / GAP_NT) * Geo_Factor * 1000;
v_model_OLEON = v_avg_model * k_loss_0;

v_avg_model_30 = sqrt(eta_OLEON) * (OLEON_base * sqrt(
    V_eff_sq_OLEON_max) / GAP_NT) * Geo_Factor * 1000;
v_model_OLEON_30 = v_avg_model_30 * k_loss_30;

figure; hold on;
plot(V_mod_max, v_x_max_exp_0, 'gd', 'MarkerFaceColor', 'g', '
    DisplayName', 'Exp. 0^\circ');
plot(V_mod_max, v_model_OLEON, 'g--', 'LineWidth', 1.5, '
    DisplayName', 'Model 0^\circ');

plot(V_mod_max, v_x_max_exp_30, 'bo', 'MarkerFaceColor', 'b', '
    DisplayName', 'Exp. 30^\circ');
plot(V_mod_max, v_model_OLEON_30, 'b:', 'LineWidth', 1.5, '
    DisplayName', 'Model 30^\circ');

ylabel('$V_{max} (mm/s)$', 'Interpreter', 'latex');
xlabel('Voltage (V)');
legend('Location', 'northwest'); grid on; box on; hold off;

%% 2. MODELO DE VELOCIDAD MEDIA
V_exp = [500, 1000, 1500, 2000, 2500, 3000, 3500, 4000, 4500,
    5000];

v_up = [0.0025, 0.0062, -0.1540, -0.3450, -0.3448, -0.7363,
    -0.9039, -1.0699, -1.4009, -1.0020]*-1;
v_down = [-0.0098, -0.0659, -0.1327, -0.3694, -0.3989, -0.6484,
    -1.0420, -1.1517, -1.4779, -1.5953]*-1;
v_m_exp = (2/3)*(v_up + v_down)/2;

```

```
v_up_30 = [-0.0530, -0.2456, -0.4629, -0.7169, -0.9710, -1.0467,
    -1.2869, -1.3638, -1.7282, -2.1582]*-1;
v_down_30 = [0.0191, 0.0696, -0.1251, -0.2498, -0.3746, -0.5445,
    -0.2769, -0.3965, -0.3971, -0.2123]*-1;
v_m_exp_30 = (2/3)*(v_up_30 + v_down_30)/2;

V_mod = linspace(0, 5000, 100);
V_diff_OLEON = V_mod - V_SCL_OLEON;
V_diff_OLEON(V_diff_OLEON < 0) = 0;
V_eff_sq_OLEON = V_mod .* V_diff_OLEON;

k_loss_0_media = 0.147;
k_loss_30_media = 0.103;

v_model_m_OLEON = sqrt(eta_OLEON) * (OLEON_base * sqrt(
    V_eff_sq_OLEON) / GAP_NT) * k_loss_0_media * Geo_Factor * 1000;
v_model_m_OLEON_30 = sqrt(eta_OLEON) * (OLEON_base * sqrt(
    V_eff_sq_OLEON) / GAP_NT) * k_loss_30_media * Geo_Factor * 1000;

figure; hold on;
plot(V_exp, v_m_exp, 'rs', 'MarkerFaceColor', 'r', 'DisplayName', '
    Exp. Results OLEON (0^\circ)');
plot(V_mod, v_model_m_OLEON, 'r--', 'LineWidth', 1.5, 'DisplayName'
    , 'Model OLEON (0^\circ)');
plot(V_exp, v_m_exp_30, 'bo', 'MarkerFaceColor', 'b', 'DisplayName'
    , 'Exp. Results OLEON (30^\circ)');
plot(V_mod, v_model_m_OLEON_30, 'b:', 'LineWidth', 1.5, '
    DisplayName', 'Model OLEON (30^\circ)');
ylabel('$V_{media} (mm/s)$', 'Interpreter', 'latex');
xlabel('Voltage (V)');
legend('Location', 'northwest'); grid on; box on; hold off;

%% 3. CALCULO Y GRAFICO DEL CAUDAL VOLUMETRICO (Q)
Q_exp_0 = (v_m_exp / 1000) * 2 * AREA_Canal * 60 * 1e6;
Q_exp_30 = (v_m_exp_30 / 1000) * 2 * AREA_Canal * 60 * 1e6;
Q_model_0 = (v_model_m_OLEON / 1000) * 2 * AREA_Canal * 60 * 1e6;
Q_model_30 = (v_model_m_OLEON_30 / 1000) * 2 * AREA_Canal * 60 * 1
    e6;

figure; hold on;
plot(V_exp, Q_exp_0, 'rs', 'MarkerFaceColor', 'r', 'DisplayName', '
    Exp. Q (0^\circ)');
plot(V_mod, Q_model_0, 'r--', 'LineWidth', 1.5, 'DisplayName', '
    Model Q (0^\circ)');
plot(V_exp, Q_exp_30, 'bo', 'MarkerFaceColor', 'b', 'DisplayName',
    'Exp. Q (30^\circ)');
plot(V_mod, Q_model_30, 'b:', 'LineWidth', 1.5, 'DisplayName', '
    Model Q (30^\circ)');
ylabel('$Q\ (mL/min)$', 'Interpreter', 'latex');
xlabel('Voltage (V)');
legend('Location', 'northwest');
grid on; box on;
hold off;
```

Listing A.2: PIV experiment code

Appendix B

Experimental Data Tables

Table B.1: Electrical characterization in air

I [mA]	V 1 [kV]	V 2 [kV]	V 3 [kV]
0,01	5,55	4,88	5,25
0,02	5,88	5,40	5,50
0,03	6,18	5,92	5,80
0,04	6,56	6,28	6,12
0,05	6,68	6,59	6,43
0,06	6,97	6,89	6,75
0,07	7,14	7,18	7,14
0,08	7,30	7,42	7,38
0,09	7,50	7,53	7,55
0,10	7,68	7,71	7,73
0,11	7,82	7,82	7,97
0,12	8,00	8,00	8,10

Table B.2: Initial test

V1 [kV]	I [μA]	H_min [mm]	H_max [mm]	H [mm]	P [Pa]
0.00	0.03	50	50	50	0.00
1.00	0.05	50	50	50	0.00
2.00	0.06	50	51	50	7.93
3.00	0.07	50	52	1	15.86
4.00	0.09	50	52	2	15.86
5.00	0.11	50	52	2	15.86
6.00	0.13	50	53	3	23.79
7.00	0.14	50	53	3	23.79
8.00	0.15	50	54	4	31.72
9.00	0.17	50	55	4	31.72
10.00	0.20	50	55	5	39.65
11.00	0.22	50	56	5	39.65
12.00	0.26	50	57	7	47.58
13.00	0.29	50	58	7	55.51
14.00	0.33	50	59	9	71.37
15.00	0.37	50	60	10	79.30
16.00	0.42	50	62	12	95.16
17.00	0.47	50	64	14	111.02
18.00	0.52	50	66	15	118.95
19.00	0.60	50	68	18	142.74
20.00	0.62	50	70	20	158.61

Table B.3: Final test

V [kV]	I [μA]	H_{min} [mm]	H_{max} [mm]	H [mm]	P [Pa]
0,00	0,04	49	49	49	0
1,00	0,05	49	49	49	0
2,00	0,06	49	49	49	0
3,00	0,07	49	49	49	0
4,00	0,08	49	49	49	0
5,00	0,09	49	50	49	1
6,00	0,11	49	50	49	1
7,00	0,12	49	51	50	2
8,00	0,13	49	53	51	7,93
9,00	0,15	49	54	52	15,86
10,00	0,17	49	54	53	31,72
11,00	0,18	49	54	53	39,65
12,00	0,21	49	54	54	47,58
13,00	0,23	49	55,5	55	56,58
14,00	0,27	49	56	56	55,51
15,00	0,29	49	57	57	63,41
16,00	0,32	49	58,5	59	75,34
17,00	0,34	49	60	60	84,24
18,00	0,44	49	62	62	103,09
19,00	0,49	49	64,5	64	122,92
20,00	0,51	49	66	66	134,81

Table B.4: Time evolution test of current and height

t [s]	t [min]	V [kV]	I [μA]	$H_{\min}$ [mm]	$H_{\max}$ [mm]	H [mm]	P [Pa]
0	0.0	15	0.04	50	50	50	0.00
30	0.5	15	0.40	50	61	11	87.23
60	1.0	15	0.41	50	60	10	79.30
90	1.5	15	0.40	50	60	10	79.30
120	2.0	15	0.40	50	60	10	79.30
150	2.5	15	0.39	50	60	10	79.30
180	3.0	15	0.38	50	60	10	79.30
210	3.5	15	0.38	50	60	10	79.30
240	4.0	15	0.37	50	59	9	71.377
270	4.5	15	0.37	50	59	9	71.37
300	5.0	15	0.37	50	59	9	71.37
330	5.5	15	0.36	50	59	9	71.37
360	6.0	15	0.36	50	58	8	63.44
420	7.0	15	0.36	50	58	8	63.44
480	8.0	15	0.35	50	58	8	63.44
540	9.0	15	0.35	50	58	8	63.44
600	10.0	15	0.35	50	58	8	63.44
900	15.0	15	0.33	50	57	7	55.51
1200	20.0	15	0.32	50	57	7	55.51
1500	25.0	15	0.31	50	57	7	55.51
1800	30.0	15	0.30	50	57	7	55.51
2100	35.0	15	0.29	50	57	7	55.51
2400	40.0	15	0.29	50	57	7	55.51
2700	45.0	15	0.29	50	57	7	55.51
3000	50.0	15	0.28	50	57	7	55.51
3300	55.0	15	0.28	50	57	7	55.51
3600	60.0	15	0.28	50	57	7	55.51

fps	tbi	V	I	# Video
30	33,33	500	0,04	1
30	33,33	1000	0,05	2
30	33,33	1500	0,05	3
30	33,33	2000	0,05	4
60	16,67	2500	0,05	5
60	16,67	3000	0,05	6
90	11,11	3000	0,05	7
90	11,11	3500	0,05	8
120	8,33	3500	0,05	9
120	8,33	4000	0,06	10
180	5,56	4500	0,06	11
180	5,56	5000	0,06	12
30	33,33	500	0,04	13
30	33,33	1000	0,05	14
30	33,33	1500	0,05	15
30	33,33	2000	0,05	16
60	16,67	2500	0,05	17
60	16,67	3000	0,05	18
90	11,11	3000	0,05	19
90	11,11	3500	0,05	20
120	8,33	3500	0,05	21
120	8,33	4000	0,06	22
180	5,56	4500	0,06	23
180	5,56	5000	0,06	24

Table B.5: PIV experimental data. During the PIV characterization, videos 1 to 12 were recorded with the camera positioned at a 30-degree tilt, whereas for videos 13 to 24, the camera was maintained at 0 degrees.

Bibliography

[1] Ronald J Adrian. "Particle-Imaging Techniques for Experimental Fluid Mechanics". In: *Annual Review of Fluid Mechanics* 23.1 (1991). DOI: 10.1146/annurev.fl.23.010191.001401.

[2] Pierre Atten, T. Honda, and F. M. J. McCluskey. "Electrical conduction and EHD motion of dielectric liquids in a knife-plane electrode assembly". In: *IEEE Transactions on Electrical Insulation* EI-20.2 (1985).

[3] Pierre Atten and Jamal Seyed-Yagoobi. "Electrohydrodynamically induced dielectric liquid flow through pure conduction in point-plane geometry". In: *IEEE Transactions on Dielectrics and Electrical Insulation* 10.1 (2003).

[4] M. Bologa and I. Kozhevnikov. "Effect of a dielectric liquid's electrization on the characteristics of an electrohydrodynamic pump". In: (2011).

[5] J. E. Bryan and J. Seyed-Yagoobi. "Experimental study of ion-drag pumping using various working fluids". In: *IEEE Transactions on Electrical Insulation* 26.4 (1991).

[6] N. Cabeo. *Filosofia Magnetica*. Ferrara, Italia, 1629.

[7] J. M. Crowley and J. C. Chato. "Selecting a Working Fluid to Increase the Efficiency and Flow Rate of an EHD Pump". In: *IEEE Transactions on Industry Applications* 26 (1990).

[8] M Daaboul et al. "Study of the transition from conduction to injection in an electrohydrodynamic flow in blade-plane geometry". In: *Journal of Electrostatics* 88 (2017). DOI: 10.1016/j.elstat.2017.01.014.

[9] M Daaboul et al. "Study of the transition from conduction to injection in an electrohydrodynamic flow in blade-plane geometry". In: *Journal of Electrostatics* 112 (2021), p. 103596. DOI: 10.1016/j.elstat.2021.103596.

[10] Michel Daaboul and Christophe Louste. "Validity of Particle Image Velocimetry Measurements in Electrohydrodynamic Flows". In: *Experimental Techniques* (2025). DOI: 10.1007/s40799-025-00806-4.

[11] J. Darabi and M. Rada. "CFD modeling of an ion-drag micropump". In: *Sensors and Actuators A: Physical* 120.1 (2005).

[12] I I Inculet and K Adamiak. "Charge limits in corona charging of distorted liquid droplets". In: *IEEE Transactions on Industry Applications* 29.6 (1993). DOI: 10.1109/28.259713.

[13] M. Jafari, N. Farrokhi, and E. Esmaeilzadeh. "Effects of working temperature and fluid physical properties on heat transfer enhancement in conduction pumping". In: (2020).

[14] LaVision GmbH. *FlowMaster Software Manual*. User manual for the PIV system. LaVision. Goettingen, Germany.

[15] F M J McCluskey and P Atten. "Velocity profiles in the injection zone of an EHD generator and efficiency considerations". In: *Conference Record of the 1985 IEEE Industry Applications Society Annual Meeting*. IEEE, 1985.

[16] J. R. Melcher. *Continuum Electromechanics*. Cambridge, MA: MIT Press, 1981.

[17] R. Mujal-Rosas et al. "Dielectric, Thermal, and Mechanical Properties of Acrylonitrile Butadiene Styrene Reinforced with Used Tires". In: *Advances in Polymer Technology* 32.S1 (2013). DOI: 10.1002/adv.21287.

[18] J Nogueira, A Lecuona, and P A Rodríguez. "Data validation, false vectors correction and derived magnitudes calculation on PIV data". In: *Measurement Science and Technology* 8.12 (1997). DOI: 10.1088/0957-0233/8/12/012.

[19] William F. Pickard. "Ion Drag Pumping. I. Theory". In: *Journal of Applied Physics* 34.2 (1963).

[20] William F. Pickard. "Ion Drag Pumping. II. Experiment". In: *Journal of Applied Physics* 34.2 (1963).

[21] H. Puago Martínez and P. Vega Martínez. "Disipador electrohidrodinámico". Pat. ES2994879B2. Patent. 2023.

[22] Markus Raffel et al. *Particle Image Velocimetry: A Practical Guide*. Berlin, Heidelberg: Springer Berlin Heidelberg, 2007. DOI: 10.1007/978-3-540-72308-0.

[23] M. Robinson. "Movement of air in the electric wind of the corona discharge". In: (1961).

[24] H. Sharbaugh and W. Walker. "The Design and Evaluation of an Ion-Drag Dielectric Pump to Enhance Cooling in a Small Oil-Filled Transformer". In: (1985).

[25] H. Stone, A. Stroock, and A. Ajdari. *Engineering Flows in Small Devices: Microfluidics Toward a Lab-on-a-Chip*. Toulouse, 2004.

[26] Otmar M. Stuetzer. "Ion drag pressure generation". In: *Journal of Applied Physics* 31.1 (1960).

[27] B. Wilson. *A treatise on electricity*. London, UK, 1752.